NUCLEAR SHELL STRUCTURE
AT VERY HIGH ANGULAR MOMENTUM

G ANDERSSON, S E LARSSON, G LEANDER, P MÖLLER, S G NILSSON,
I RAGNARSSON and S ÅBERG

Lund Institute of Technology, Lund, Sweden

R BENGTSSON [†]

NORDITA, Copenhagen, Denmark

and

J DUDEK [††], B NERLO-POMORSKA [†††], K POMORSKI [†††] and Z SZYMAŃSKI

Institute for Nuclear Research, Warsaw, Poland

Received 6 April 1976

Abstract: A cranked modified-oscillator model (with triaxial shape coordinates ε and γ) is used to study the nuclear potential-energy surface (based on a Strutinsky type of shell correction method) for very high angular momenta ($30 \leq I \leq 100$) For this region of spin, pair correlation is assumed to have collapsed The influence of rapid rotation on the shell structure has been studied in the light and heavy rare-earth region as well as the Te-Ba region Preliminary studies have also been made in the regions of superheavy and light nuclei The possible occurrence of yrast traps is discussed

1. Introduction

The sequence of nuclear states, each characterized as being the lowest-energy state of each spin, is called the "yrast" band. Presently such yrast states are positively identified up to band members of $I = 20$ and greater, usually in the prolate deformed region, while there are indications that yrast transitions involving spin members of the order of 60 units of $\hbar$ have been observed [1] (for ^{118}Te). The back-bending region, which for deformed rare-earth nuclei usually occurs between $I = 10$ and 16, is thought to involve both a change of intrinsic pair correlation and an orbital realignment implying a loss of axial symmetry, although modest non-axial distortions are involved in the alignment In the spin region above $I = 25$ there are indications of not one dominant yrast cascade but of several parallel ones. This is also an indication of a nuclear γ deformation i.e. a non-axial shape [2]. At higher spin values the liquid-drop model may be taken to indicate a stably oblate spin region which is realised, in existing nuclei, only in special regions of mass For still higher spins there is again a

---

[†] On leave from the Lund Institute of Technology, Lund, Sweden
[††] University of Warsaw, Warsaw, Poland
[†††] The Maria Skłodowska-Curie University, Lublin, Poland

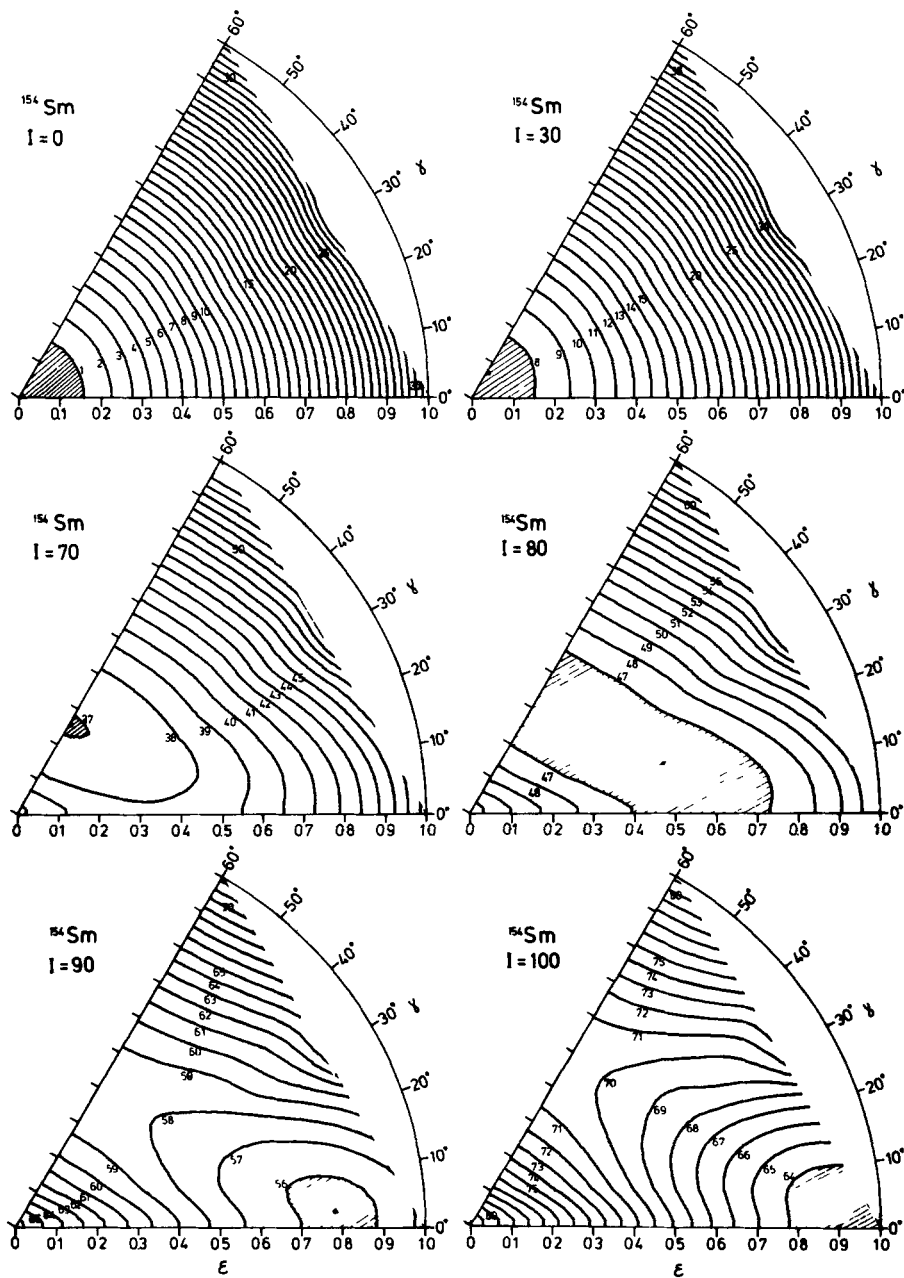Fig 1　Potential-energy surfaces for ^{154}Sm at different total angular momentum I in terms of ε (elongation) and γ (axial) asymmetry　The energy (denoted "liquid-drop energy") is calculated as a sum of Coulomb and surface energy in addition to the energy of rigid rotation　In each grid point a minimisation with respect to ε_4 is applied

trend towards triaxiality. The termination of the yrast band is for heavy elements usually decided by the instability to fission. This instability comes about because the resistance to deformation, provided by the increase in surface energy, is overcome by the decrease in rotational energy, due to the increase in the moment of inertia value with deformation. Also other processes may terminate the yrast band at still lower angular momentum. Examples of such terminating effects are instabilities to α-decay or neutron emission.

A broad survey of the behaviour of the yrast band with I can be found in the paper by Bohr and Mottelson [3]), contributed to the Ronneby conference on superheavy elements in 1974. Some of its conclusions were based on the calculations involving the rotating liquid-drop model by Cohen, Plasil and Swiatecki [4]), then already available. The present paper has the same theme as that outlined in ref. [3]) and the conclusions, based on a model fusing liquid-drop and shell effects, are found to bear
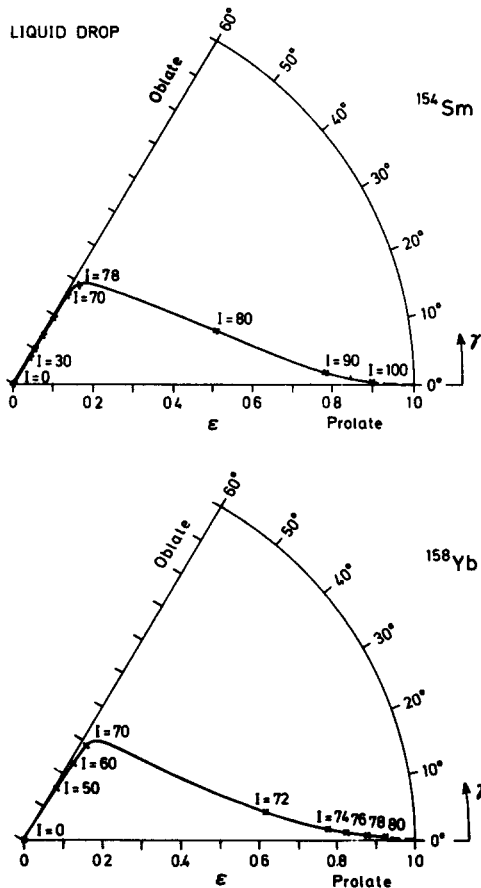

Fig 2 The rotating "liquid-drop" minimum shape in terms of ε and γ (also ε_4 implied) as a function of total angular momentum I for ^{154}Sm and ^{158}Yb ($x = 0.510$ and 0.618 respectively)

out to a large extent what is conjectured in ref. [3]). Some preliminary results of the present calculations were published in ref. [5]). They are in good agreement with the independent results obtained by Neergaard, Pashkevich and Frauendorf [6,7]) based on a very similar model.
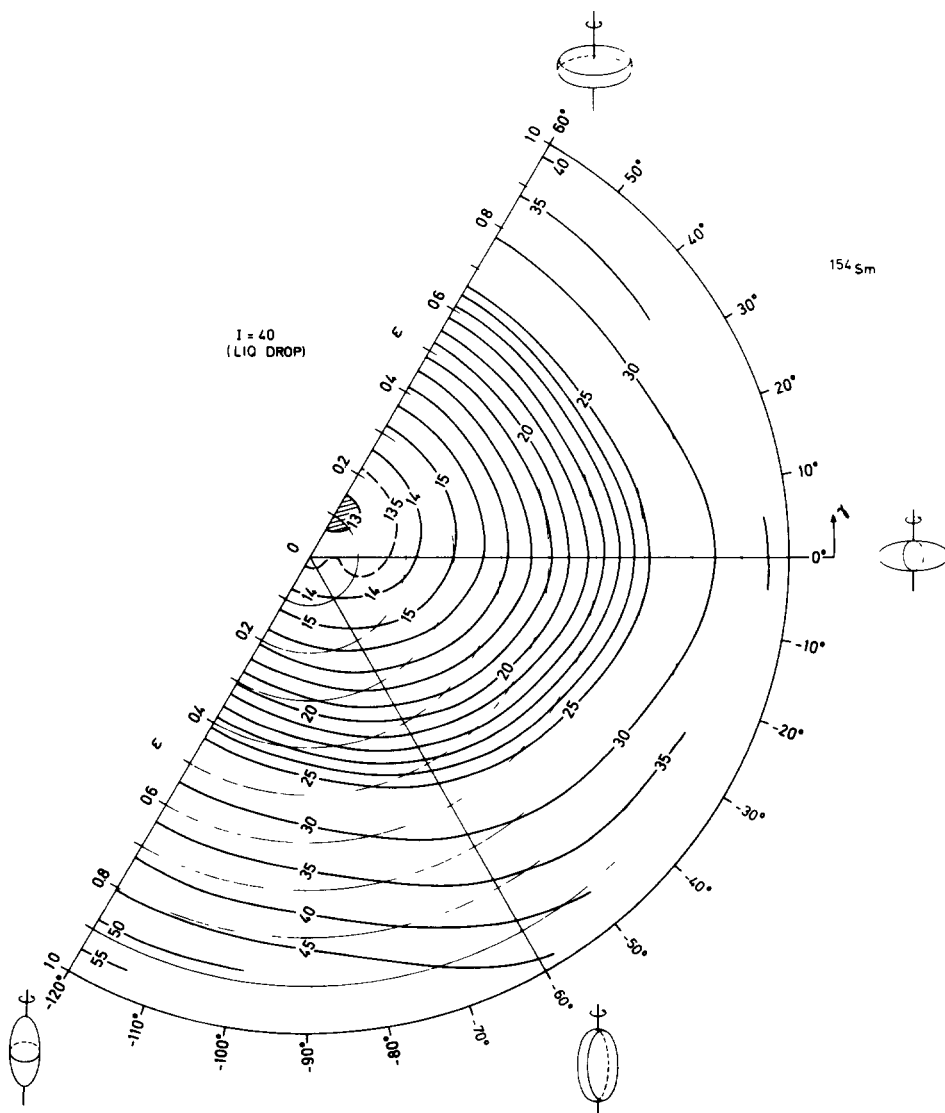

Fig 3 The rotating "liquid-drop" energy surface for ^{154}Sm, $I = 40$ in terms of three sextants of ε and γ (with a minimisation with respect to ε_4 implied)

2. The liquid-drop description of nuclei

In the cited paper by Cohen, Plasil and Swiatecki [4]) a study is made of the classical problem of deformation and rotation. Here the nucleus is characterized by a Coulomb energy term corresponding to a homogeneous charge, a surface energy term strictly proportional to the surface area and a rotation energy term corresponding to rigid rotation. We refer the reader to this excellent study. Our first attempt was to reproduce the results there obtained but in terms of the ε, ε_4, γ representation defined in the modified-oscillator model [8]). In fig. 1 we exhibit the energy surfaces for ^{154}Sm corresponding to six different values of angular momentum I. In fig. 2 we give the corresponding trajectories in the ε, γ plane for ^{154}Sm and ^{158}Yb. One should note that in this calculation a minimization with respect to ε_4 is made in each grid point of ε and γ.

As long as only rigid rotation is considered for the classical problem, only the sector $0 \leq \gamma \leq 60°$ needs to be considered as indeed the largest inertia is obtained for a rotation around the x-axis. This is well illustrated in fig 3 giving an entire three-sector energy surface, where it is thus assumed that rotation takes place around the x-axis. The moment of inertia with respect to the x-axis turns out to be the largest, the middle one and the smallest of the three principal inertia values, respectively, in the three sectors One should note that fig. 3 is applicable only for the case of rigid rotation. With an alternative assumption of irrotational flow, e g. as considered by Meyer-ter-Vehn [9]), it is obvious that the largest inertia and the smallest energies are obtained for negative values of γ, involving a flattening of the prolate nucleus perpendicular to the plane of the symmetry axis and the rotation axis x.
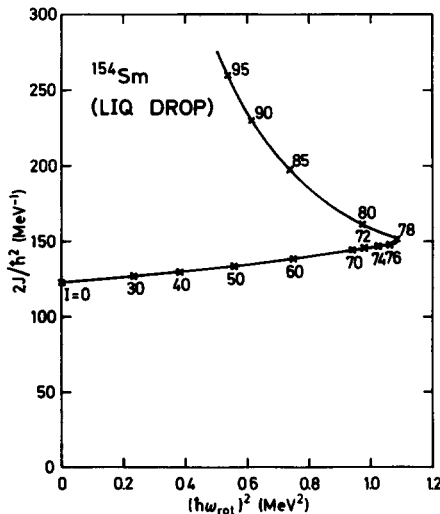

Fig 4 Diagram of the moment of inertia term $\partial E/\partial I^2$ versus the square of the rotational frequency term $(\partial E/\partial I)^2$ for the calculated yrast spectrum of ^{154}Sm in terms of the rotating "liquid-drop" model

Returning to the classical rigid rotation problem, from the associated angular momenta, energies and shapes one may construct a classical yrast plot, as that given in fig. 4 for ^{154}Sm, where the rotation angular velocity and the moment of inertia are defined as

$$\hbar\omega = \frac{\partial E}{\partial I}, \qquad \frac{\hbar^2}{2\mathscr{I}} = \frac{\partial E}{\partial I^2}.$$

One apparent feature is the strong "super-back-bend", also noted by Swiatecki and coworkers [1,10], at spin 78. This feature of the spectrum appears to persist even when shell structure effects are included. For the transitions $I+2 \rightarrow I$ it leads to a frequency "pile-up" [1] i.e. a situation where the transition energies no more increase with I in the region above $I = 78$

3. The single-particle orbitals in the rotating system

For the zero angular momentum case one considers an independent-particle Hamiltonian

$$H^0 = \sum_i h_i^0.$$

Here h_i^0 is the single-particle Hamiltonian where residual two-body interactions, as the pairing interaction, have been neglected. The assumption of pairing collapse is an appropriate approximation only for I-values in excess of 20–30 in this region of mass, as indicated by the HFB calculations with pairing explicitly included by the Faessler group [11]. For the problem of higher angular momentum one considers the auxiliary Hamiltonian

$$H^\omega = H^0 - \hbar\omega I_x,$$

where one may consider $\hbar\omega$ a Lagrangian multiplier introduced for the fulfilment of the condition of a given expectation value of I_x

$$\langle I_x \rangle = I.$$

Here quantum mechanical wobbling can obviously be neglected for large I. One may also consider $\hbar\omega I_x$ the Hamiltonian form of the summed Coriolis and centrifugal terms of a system rotating with the frequency ω. The quantity H^ω is then the Hamiltonian describing the field of the nucleons in the rotating system. Obviously only the modification due to the kinetic energy terms is taken into account. The influence of rotation on two-particle interactions is considered in ref. [7].

Also the "generator" Hamiltonian H^ω is a sum of one-body operators

$$H^\omega = \sum_i h_i^\omega = \sum_i (h^0 - \hbar\omega j_x)_i.$$

For the static single-particle Hamiltonian $h^0 = T + V$ we employ a modified harmonic

oscillator (MO) with

$$V = \tfrac{1}{2}\hbar\omega_0\rho^2[1 - \tfrac{2}{3}\varepsilon\sqrt{\tfrac{4}{5}\pi}(\cos\gamma)Y_{20} + \tfrac{2}{3}\varepsilon\sqrt{\tfrac{4}{5}\pi}\sqrt{\tfrac{1}{2}}\sin\gamma(Y_{22} + Y_{2-2})]$$
$$- \hbar\omega_0[2\kappa l_t \cdot s + \mu'(l_t^2 - \langle l_t^2\rangle)].$$

In the rotating case the remaining symmetries of the problem are only parity and rotation an angle π around the x-axis, the latter symmetry exploited by the operator $\exp(i\pi j_x)$.

In our calculations so far, the coupling between different "stretched" N_t shells due to the $\hbar\omega j_x$ term is neglected. From the diagonalization of the problem

$$h_i^\omega \chi_i^\omega = e_i^\omega \chi_i^\omega,$$

modified eigenfunctions are obtained. The corresponding "real" energies are subsequently calculated as expectation values

$$\langle e_i\rangle = \langle \chi_i^\omega | h^0 | \chi_i^\omega\rangle = e_i^\omega + \hbar\omega\langle \chi_i^\omega | j_x | \chi_i^\omega\rangle = e_i^\omega + \hbar\omega\langle m_i\rangle,$$

and correspondingly the total energy as a sum of expectation values

$$E_{\text{s p}} = \sum_i \langle e_i\rangle = \sum_i e_i^\omega + \hbar\omega\sum_i \langle m_i\rangle = \sum_i e_i^\omega + \hbar\omega I,$$

where thus $\langle m_i\rangle = \langle \chi_i^\omega | j_x | \chi_i^\omega\rangle$. Note here that the order of level occupation is determined from the order of the e_i^ω.

Two cases are particularly interesting, the purely oblate, $\gamma = 60°$, and the purely prolate, $\gamma = 0°$. For the $\gamma = 60°$ case the rotation axis is a symmetry axis and $j_x = m$ a constant of the motion. Although there is no collective rotation about the symmetry axis, every nucleon contributes its individual angular momentum j_x to the total spin I. Since $j_x = m$ is a good quantum number we have the same eigenfunctions of h^0 and h^ω, i.e.

$$\chi_i^\omega = \chi_i \qquad (\gamma = 60°),$$

$$e_i^\omega = e_i - \hbar\omega m_i \qquad (\gamma = 60°).$$

It appears to be convenient to add explicitly the particle number operator A and to introduce the corresponding Lagrange multiplier λ. The last equation can thus be replaced by

$$e_i^\omega - \lambda = e_i - \hbar\omega m_i - \lambda,$$

thus corresponding to a "sloping" (with m) Fermi surface in the e-case. The total energy $E_{\text{s p}}$ is now calculated as a sum

$$E_{\text{s p}} = \sum_i e_i,$$

where the summation extends over A-states for which the values of $e_i^\omega - \lambda$ are the

lowest possible; say negative

$$e_i < \hbar\omega m_i + \lambda.$$

The configuration thus defined is referred to as "optimal". The two Lagrange multipliers $\hbar\omega$ and λ are then determined for the total angular momentum I and the condition
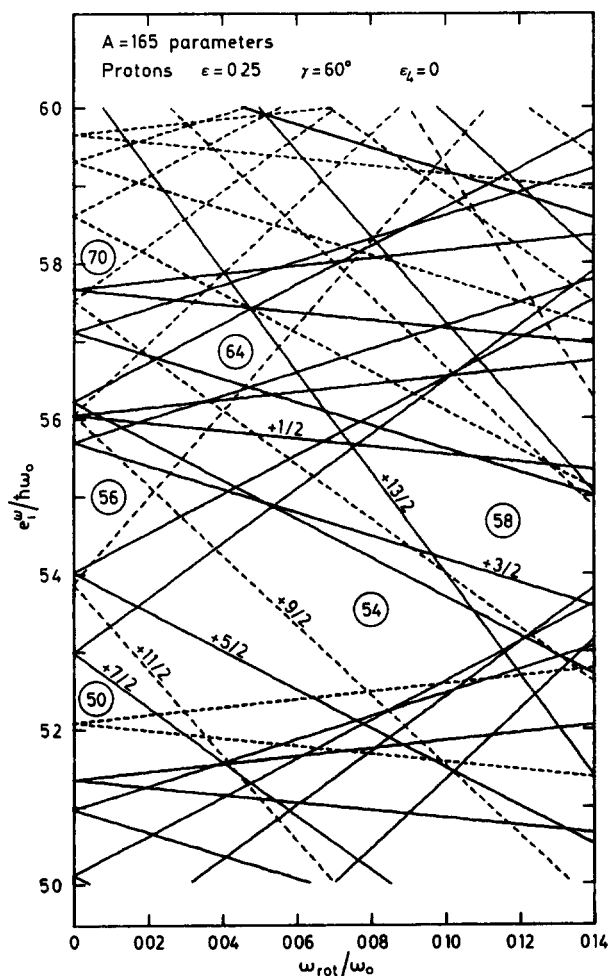
$$\sum_i 1 = A,$$

Fig 5 Single-particle energies e_i^{ω} (in "rotating system") for pure oblate $\gamma = 60°$ as a function of the rotation frequency ω expressed in units of the oscillator frequency ω_0 The solid and dashed lines correspond to eigenvalues $+1$ and -1, respectively, of the operator $\exp(i\pi j_x)$

with the summation running over all the occupied states i.e. those fulfilling the inequality for e_i given above.

It is now easy to plot the single-particle energies as functions of ω, as every time-reversal degeneracy occurring for $\omega = 0$ is split by ω into two straight lines, the slopes of the lines being given by the constant angular momentum components $+m$ and $-m$. An example of such a diagram is given in fig. 5, valid for rare-earth protons at $\varepsilon = 0.25$ and $\gamma = 60°$. Another instructive presentation of the same relationship is provided in fig. 6, where the single-particle orbitals are plotted, for $\varepsilon = 0.75$ and $\gamma = 60°$, according to energy e_i and angular momentum component m_i. The level filling is now governed by a "sloping Fermi surface", as depicted in this figure.
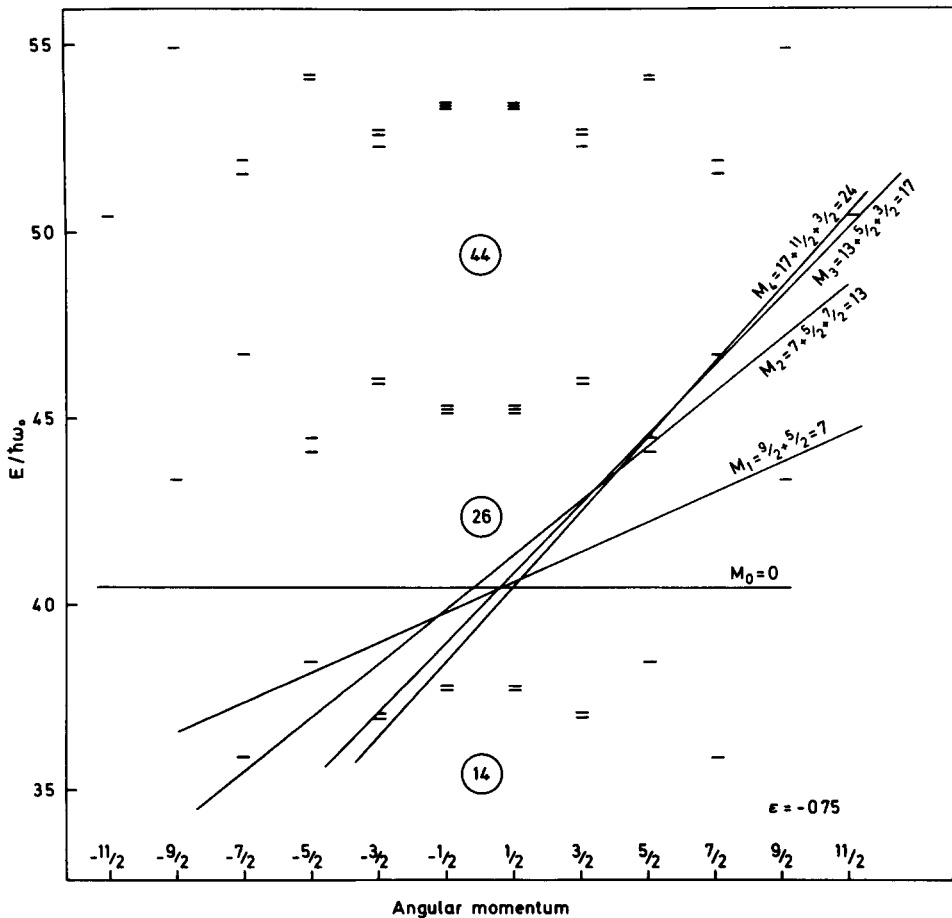

Fig 6 Pure oblate ($\gamma = 60°$, $\varepsilon = 0.75$) single-particle energy spectrum e_i (measured in oscillator energy units) versus angular momentum component m_i for the modified-oscillator model. Differently sloping Fermi surfaces correspond to different values of $I = M = \sum m_i$. The picture corresponds to the MO model with $\kappa = 0.075$ and $\mu = 0.213$, valid for neutrons in the $A = 50$ region.

Another interesting region of shapes is that of the pure prolates. Here the expectation value of $\langle j_x \rangle$ is identically zero for $\omega = 0$. Already for infinitesimally small ω the $j_z = \Omega = \frac{1}{2}$ states exhibit non-vanishing $\langle j_x \rangle$ values. The $|\Omega| = \frac{1}{2}$ states therefore immediately split with ω, subsequently the $|\Omega| = \frac{3}{2}$ states split (by coupling to the $|\Omega| = \frac{1}{2}$ ones) and then the $|\Omega| = \frac{5}{2}$ states, etc. This can be studied in fig. 7, valid for protons with $\varepsilon = 0.20$, $\gamma = 0°$. Another series of plots shows how the orbitals gain angular momentum (along the rotation axis) with increasing ω; figs. 8 and 9.

Some detailed technical problems associated with the calculations are exemplified in figs. 10 and 11. The examples are taken from the light (Ne–Mg) deformed region. In fig. 10 we plot the values e_i^ω for single-particle orbitals in the ^{24}Mg region for $\varepsilon = 0 40$ and $\gamma = 0$. The solid and dashed lines correspond to different eigenvalues with respect to the exp $(i\pi j_x)$ operator.

In fig 11b is plotted the corresponding diagram of $E_{s\,p}$ for ^{24}Mg as a function of ω. In this case the levels are assumed identical for neutrons and protons. We shall therefore always assume for simplicity that if a neutron is lifted to another level, the same happens with the proton. Although a crossing of two levels of different parities are involved, we thereby describe only even-parity states. The curve $E_{s\,p}$ is piecewise
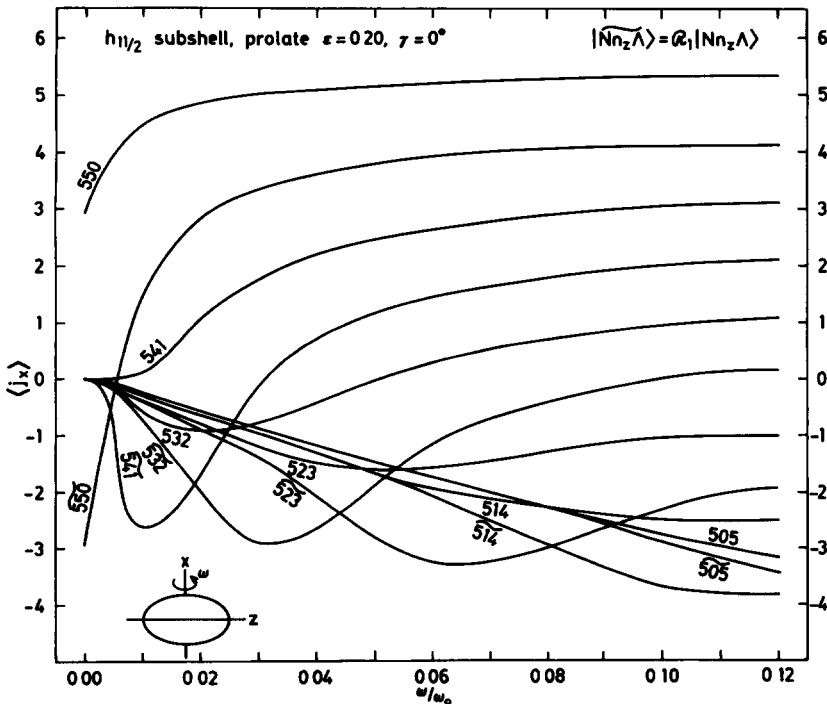

Fig 7 Single-particle angular momentum component along the rotation axis $\langle j_x \rangle$ for orbitals of the $h_{11/2}$ subshell for the pure prolate $\varepsilon = 0 20$, $\gamma = 0°$ case as a function of the rotation frequency ω Note the increasing alignment with respect to the x-axis, commencing with the $j_z = \Omega = \frac{1}{2}$ orbitals
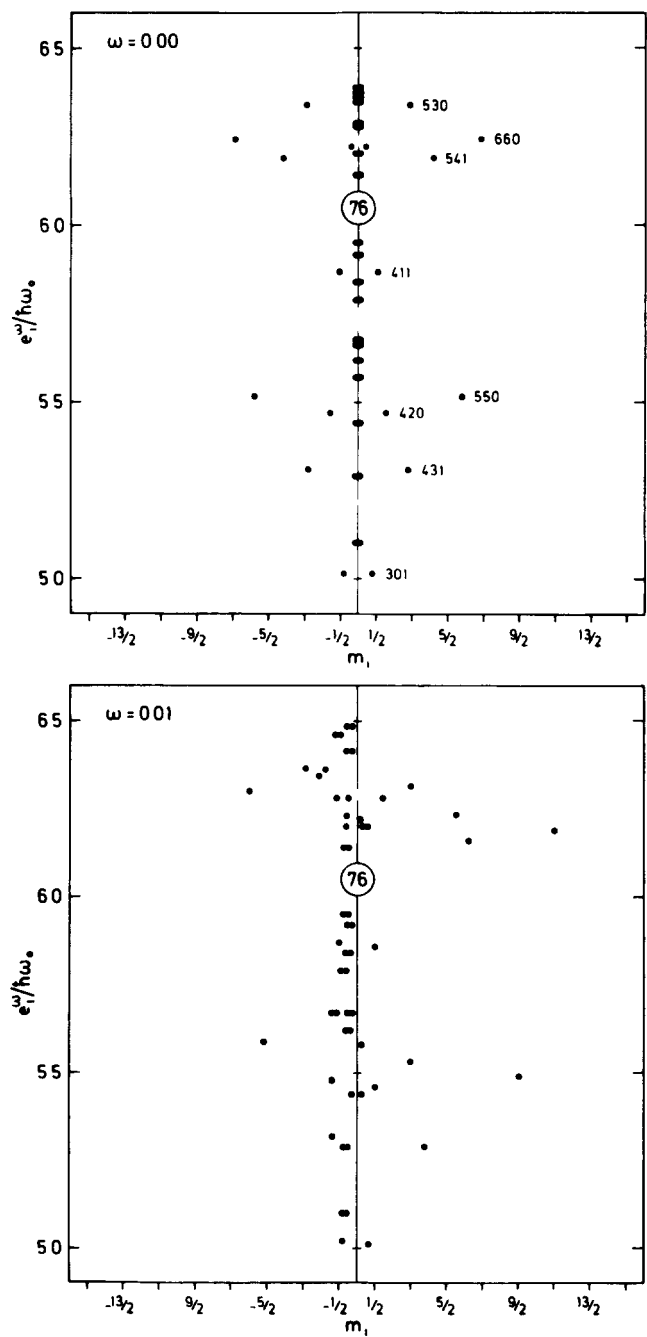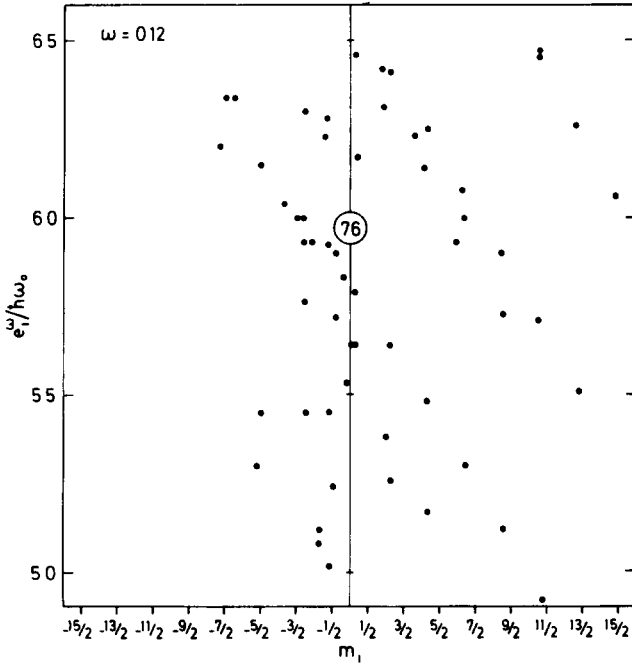
Fig. 8a

Fig 8b

Fig 8 Single-proton energies e_i^ω in the rare earth region for pure prolate $\varepsilon = 0\ 20$, $\gamma = 0$ plotted versus the component of angular momentum aligned along the x-axis, $\langle J_x \rangle$, for three values of the rotation frequency ω Note that for infinitesimally small ω, denoted $\omega = 0\ 00$ only the $J_z = \Omega = \frac{1}{2}$ states show a non-vanishing component of $\langle J_x \rangle$

continuous. The discontinuities correspond to the crossing points of the e^ω curves as functions of ω, occurring at the Fermi surface. Thus, just at the point where one orbital is unfilled and another filled, their e_i^ω values coincide. However, their $\langle e \rangle_i$ values differ leading to the discontinuity in $E_{s\ p}$ versus ω The same discontinuities occur for I versus ω, as is shown in fig. 11a valid for the same nuclide and distortion. From the latter two curves one may construct the final one of $E_{s\ p}$ versus I, as shown in fig. 11c. The discontinuities in $E_{s\ p}(\omega)$ and $I(\omega)$ are now exhibited as disconnections in the curve $E_{s\ p}(I)$.

An interesting problem is how the resulting gaps are to be filled. Obviously, if the particle is left in the initially filled orbital after passing through an e_i^ω level intersection, the $E_{s\ p} = E_{s\ p}(I)$ curves are continued, as shown by the·dashed curve pieces in fig. 11c. Finally the curve continuations from left and right meet and intersect.

4. The Strutinsky method for the $\omega \neq 0$ case

In principle a complete mapping is made of the energy for given I as a surface in deformation space. From the minima of this surface a "physical" yrast band may be
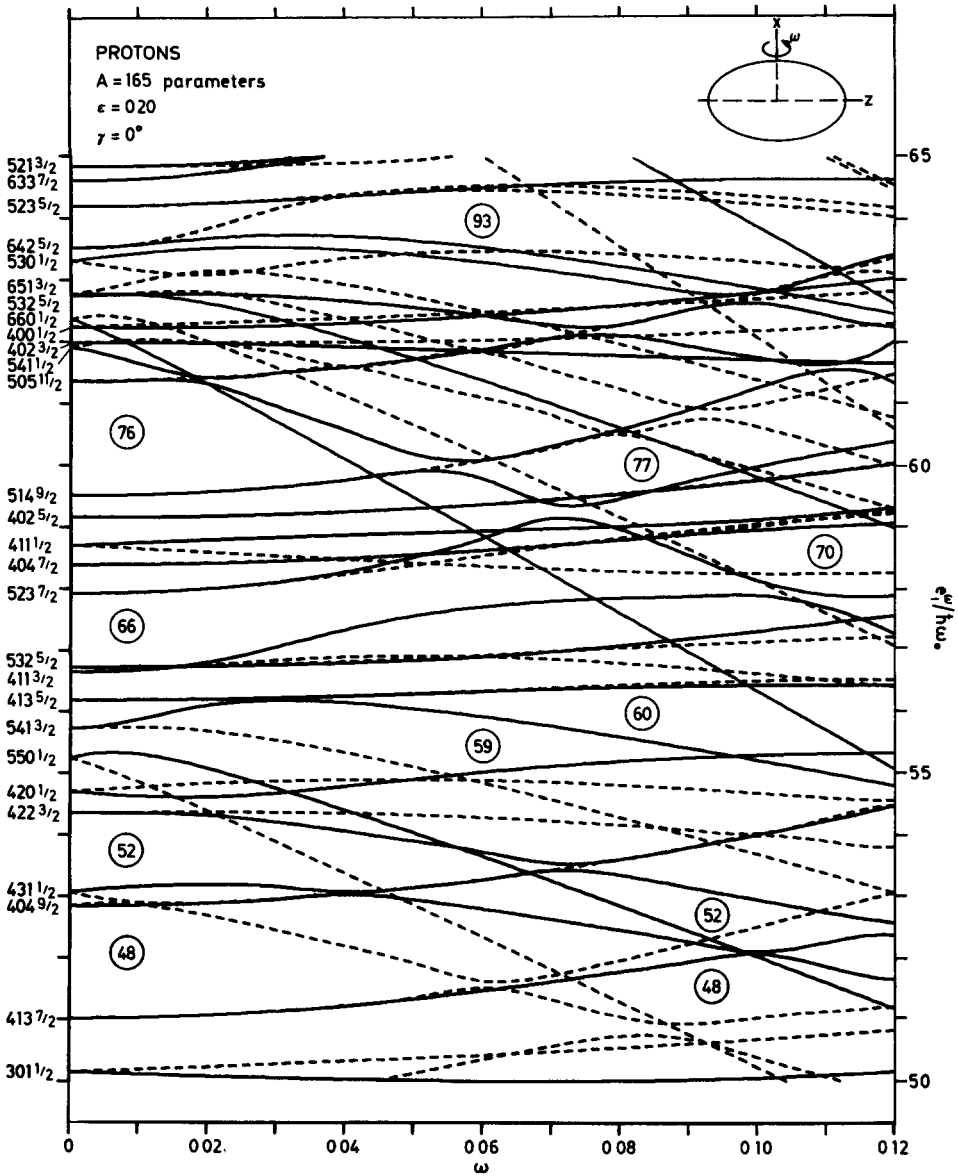
Fig 9 Single-proton energies e_i^ω in the rare-earth region for a pure prolate case $\varepsilon = 0\,20$, $\gamma = 0$ Note the level splitting into one dashed and one solid orbital denoting the eigenvalues $+1$ and -1, respectively with respect to $\exp(i\pi j_x)$
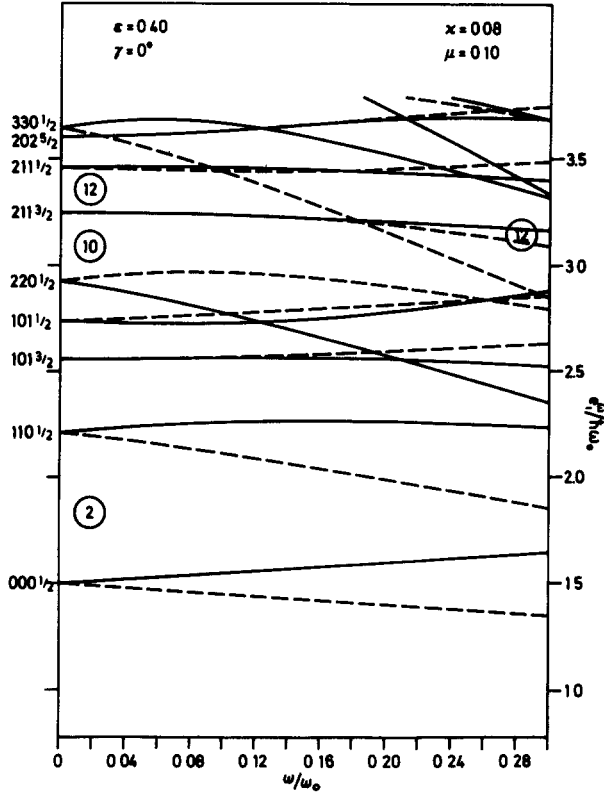
Fig 10 Single-nucleon levels e_i^ω in the (s, d) shell region for $\varepsilon = 0\,40$, $\gamma = 0°$ For notation see fig 9

constructed. It is to be noted that for the $I = 0$, $\omega = 0$ case, according to experience, the energy surface is reliable first when a Strutinsky renormalisation has been applied.

Thus to compare the total energies of largely different shapes the single-particle energy sum with corrections for pairing and Coulomb repulsion is found to need the renormalisation to the liquid drop average behaviour.

Such a renormalisation also appears necessary in the MO case in order to describe the rise in energy as a function of angular momentum for the single-particle potential employed. The Strutinsky smearing in this case, contrary to the case of $\omega = 0$, has to keep account of both the *level density and the angular-momentum density*. In this way we form, in line with a formulation suggested by Jennings [12]), a level density function

$$g_1(e^\omega) = \int_{-\infty}^{\infty} dm g(e^\omega, m) = \sum_i \delta(e^\omega - e_i^\omega),$$
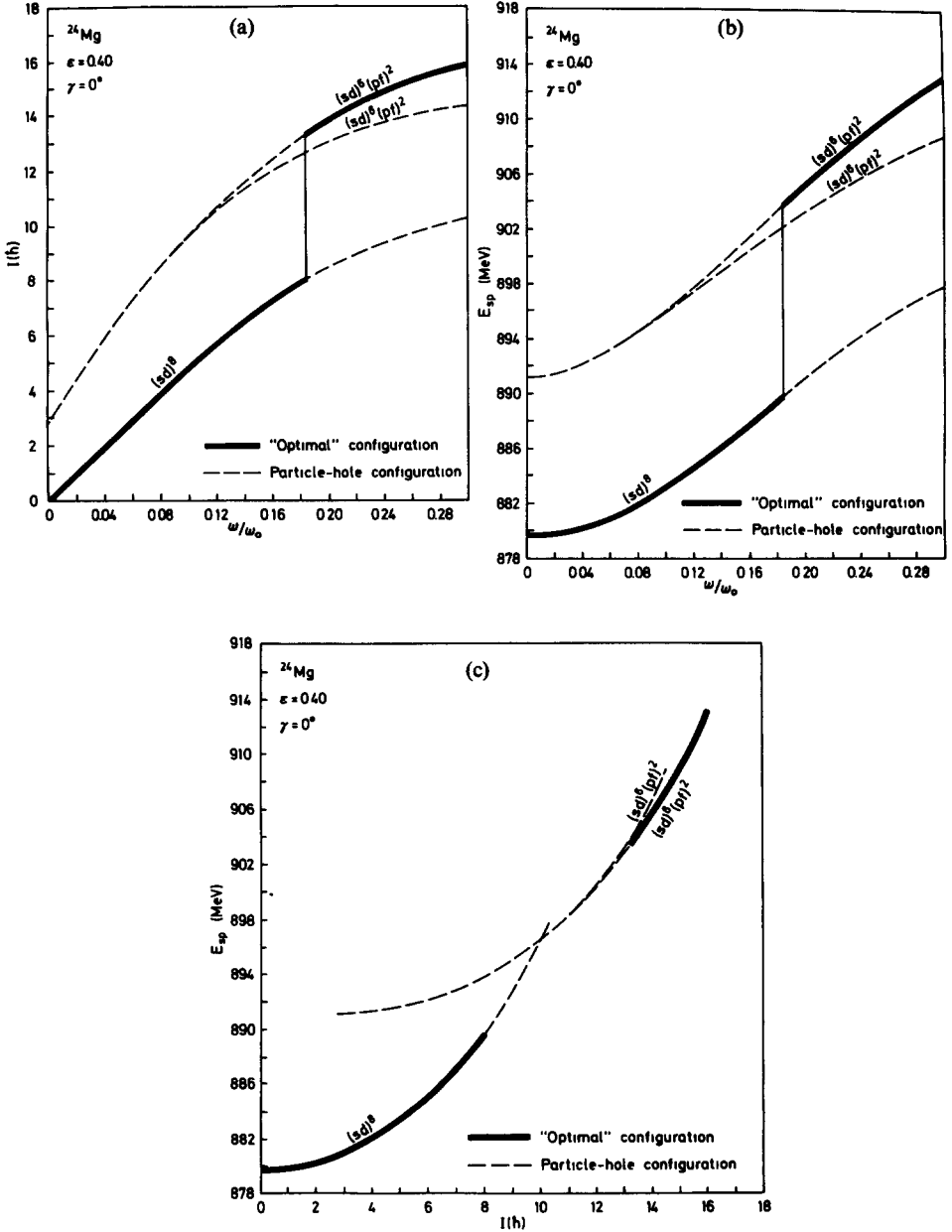
Fig 11 The relations between rotation frequency ω, energy and spin The levels of fig 10 are assumed to be filled from the bottom by twelve neutrons and twelve protons For low ω the configuration in the (s, d) shell is $(sd)^8$ Level crossings in fig 10 for $\omega/\omega_0 \approx 0\,18$ give rise to configuration $(sd)^6(pf)^2$ and a discontinuous increase in I as well as $E_{s\,p} = \sum\langle e_i\rangle$ In the E versus I plot this leads to a curve gap or a "non-optimal" region between $I = 8$ and 13. Note that only simultaneous excitations of neutrons and protons are considered.

and a spin density function

$$g_2(e^\omega) = \int_{-\infty}^{\infty} m\,dm\,g(e^\omega, m) = \sum_i \langle m_i \rangle \delta(e^\omega - e_i^\omega).$$

The corresponding Strutinsky smeared density functions are

$$\tilde{g}_1(e^\omega) = \int_{-\infty}^{\infty} S(e^\omega - \varepsilon^\omega) g_1(\varepsilon^\omega)\,d\varepsilon^\omega,$$

$$\tilde{g}_2(e^\omega) = \int_{-\infty}^{\infty} S(e^\omega - \varepsilon^\omega) g_2(\varepsilon^\omega)\,d\varepsilon^\omega$$

Here $S(e^\omega - \varepsilon^\omega)$ denotes the Strutinsky smearing function. From g_2 and g_1 we obtain the angular momentum and energy, respectively. In the discrete case

$$I = \int_{-\infty}^{\lambda} g_2\,de^\omega = \sum_{occ} \langle m_i \rangle,$$

where λ is obtained from the particle number required. Furthermore we have

$$E_{s\,p} = \int_{-\infty}^{\lambda} g_1 e^\omega de^\omega + \hbar\omega \int_{-\infty}^{\lambda} -g_2\,de^\omega = \sum e_i^\omega + \hbar\omega I.$$
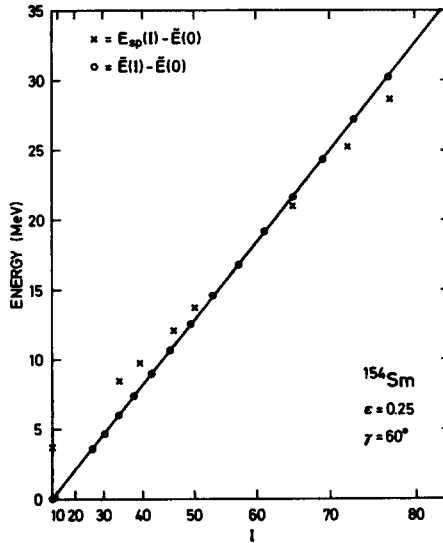

Fig. 12 Sum of single-particle energies $E_{s\,p} = \sum \langle e_i \rangle$ versus I for discrete levels (crosses) and Strutinsky smeared levels (circles) $\tilde{E}(I)$. The difference measures the shell energy
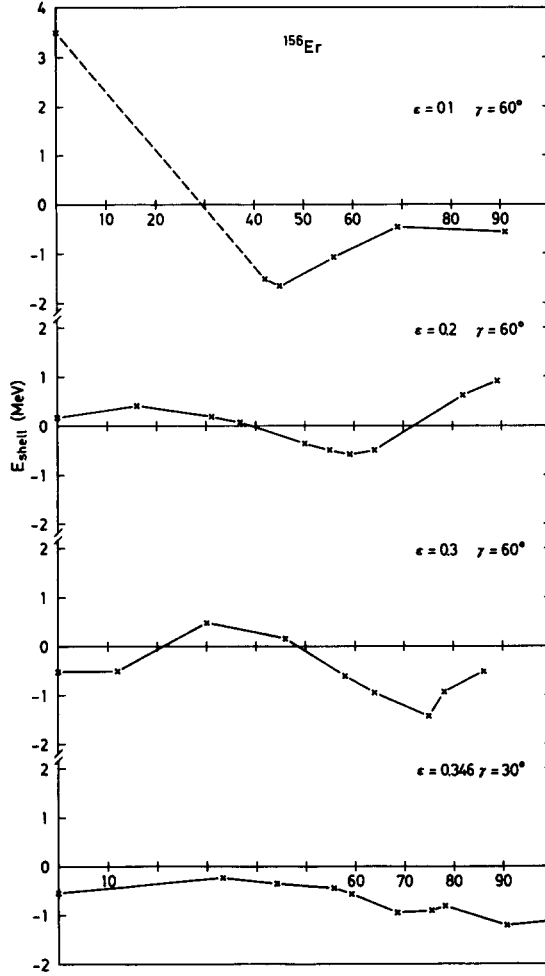
Fig 13 The shell energy for ^{156}Er as a function of I for four different distortions Note the period of E_{shell} of about 100 units of angular momentum

Similarly from the Strutinsky smeared functions $\tilde{g}_1$ and $\tilde{g}_2$ we obtain

$$\tilde{I} = \int_{-\infty}^{\tilde{\lambda}} \tilde{g}_2 de^{\omega},$$

$$\tilde{E} = \int_{-\infty}^{\tilde{\lambda}} \tilde{g}_1 e^{\omega} de^{\omega} + \hbar\omega\tilde{I}.$$

One should be aware that in the calculations E_{shell} is evaluated for constant I and not for constant ω. It is true that technically one given value of ω results in the discrete-level case in a pair of values $E_{s.p}$ and I, and in the smeared-level case in a
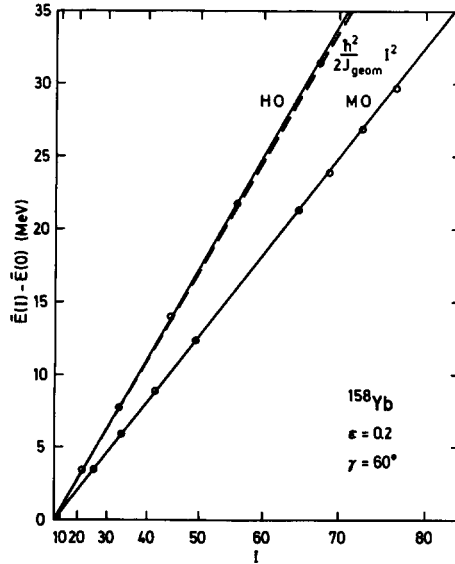
Fig 14   The total energy based on Strutınsky smeared levels $\tilde{E}(I) - \tilde{E}(0)$ for the nucleus ^{158}Yb at $\varepsilon = 0$ 20, $\gamma = 0°$ for the pure harmonıc oscıllator (HO) and the modıfied-oscıllator case (MO) compared wıth the macroscopıc rotatıonal energy based on the so-called geometrıc (or rıgıd) ınertıa value   The latter ınertıa corresponds to that of a rıgıd body wıth the shape correspondıng to an equıpotentıal surface

pair $\tilde{E}$ and $\tilde{I}$. The shell energy $E_{\text{shell}}(I)$ ıs then obtaıned as the dıfference for constant $I(=\tilde{I})$, and *not* [†] constant ω, between the fluctuatıng function $E_{\text{s p}}$ and the smooth function $\tilde{E}$. As ω has no precıse physıcal meanıng ın the dıscrete case, we prefer to refer everythıng to the relatıon between $E_{\text{s p}}$ and I.

Fig. 12 ıs a plot of $E_{\text{s p}}$ versus I^2 ın the dıscrete case and $\tilde{E}$ versus $\tilde{I}^2$ ın the smeared case. One first notes that $\tilde{E}$ versus $\tilde{I}^2$ follows a very nearly straıght lıne. In fact the lıne ıs so close to a straıght lıne that for ıts determınatıon we have ın most cases been content wıth the calculatıon of two or three poınts. The poınts correspondıng to the dıscrete levels are scattered above and below thıs straıght "macroscopıc" lıne.

The dıfference between the poınts and the lıne, although only defıned for a few dıscrete I-values, ıs consıdered to be the true "shell energy functıon" (defıned ın terms of I). It ıs assumed that ıt ıs also defıned ın ıntermedıate poınts by ınterpolatıon provıded the set of ω-values ıs chosen suffıcıently dense. In our case we have used ten ω-values, namely $\omega = 0, 0.04\ (0.01)\ 0.12$ ın units of the oscıllator frequency $\dot{\omega}_0$. The so-defıned shell-correctıon functıon ın the mass regıon of $A \approx 150$ ıs found to have a perıod ın I of 50–100 units and thus change sıgn usually over 30 to 50 units of angular momentum, dependent on deformatıon. Samples of shell energy functıons valıd for ^{156}Er and $(\varepsilon = 0.1, \gamma = 60°)$, $(\varepsilon = 0.2, \gamma = 60°)$, $(\varepsilon = 0.3, \gamma = 60°)$ and $(\varepsilon = 0.346, \gamma = 30°)$, respectıvely, are gıven ın fig. 13.

[†] Wıth Neergaard *et al* [6]) one mıght alternatıvely thus speak of two "correctıons" one to $E_{\text{s p}}$ defıned as $\delta E = E_{\text{s p}} - \tilde{E}$ for gıven ω and $\delta I = I - \tilde{I}$, also for gıven ω

5. The "dynamical" inertia values obtained for Strutinsky smeared single-particle levels

In fig. 14 we have plotted $[\tilde{E} - \tilde{E}(I = 0)]$ as a function of I^2 for the nucleus ^{158}Yb for single-particle levels obtained from the modified-oscillator (MO) potential used here, containing an $[l^2 - \langle l^2 \rangle]$ term. The slope is inversely proportional to an inertia value which we shall define as the "dynamical". For comparison also the case of the pure oscillator (HO) is given. Finally a dashed line is drawn representing the inverted "geometrical" moment of inertia expression, denoted $\hbar^2/2J_{geom}$, and corresponding to a homogeneous mass distribution inside an equipotential surface. This inertia is within 1 or 2 % the same as the "static" inertia value defined as the expectation value of $x^2 + y^2$ over the matter distribution generated by the wave functions.

It is furthermore found that the "static" inertia agrees with the "dynamic" one for the pure HO case. This agreement has also been verified by us for the infinite square well and, in a few cases, for a Woods-Saxon type potential. The deviation in the MO case is found to be of the order of 30 % as we noted in ref. [5]), when the $\langle l^2 \rangle$ term is retained, and about 70 % without this term. This can easily be understood in a qualitative way, as shown by Mottelson [13]), Brack et al. [14]) and independently by Neergaard et al. [7]). The problem is treated in more detail in the appendix. Furthermore the $l \cdot s$ term contributes about 3 % to J_{dyn}

The deviation is thus due to the velocity dependent terms of the MO potential, originally introduced to simulate static radial shape corrections to the HO potential. We therefore deem it as most appropriate to subtract the average "macroscopic" inertia obtained from the Strutinsky smeared level structure and replace it with the "static" or "geometric" value. This procedure is in line with the general philosophy of the Strutinsky type of calculation.

6. The total-energy surface

We are now in a position to construct the total-energy surface. This is obtained from

$$E_{tot}(\varepsilon, \gamma) = E_{macr}(\varepsilon, \gamma, \min \varepsilon_4) + E_{shell}(\varepsilon, \gamma).$$

Note that at the moment we are content with using ε_4 only for the macroscopic term, the sum of Coulomb, surface and rotational-energy terms. The liquid-drop model constants are chosen according to Myers and Swiatecki [15]). In the diagrams shown, E_{shell} is obtained for a grid of deformation points in ε and γ with $\varepsilon_4 = 0$.

Calculations are up to now completed in the light and heavy rare earth regions, the Te region near $A \approx 120$, in progress in the Ne–Mg region, and the superheavy region near $Z = 114$, $N = 184$. We discuss below the first two regions in more detail, the others only briefly.
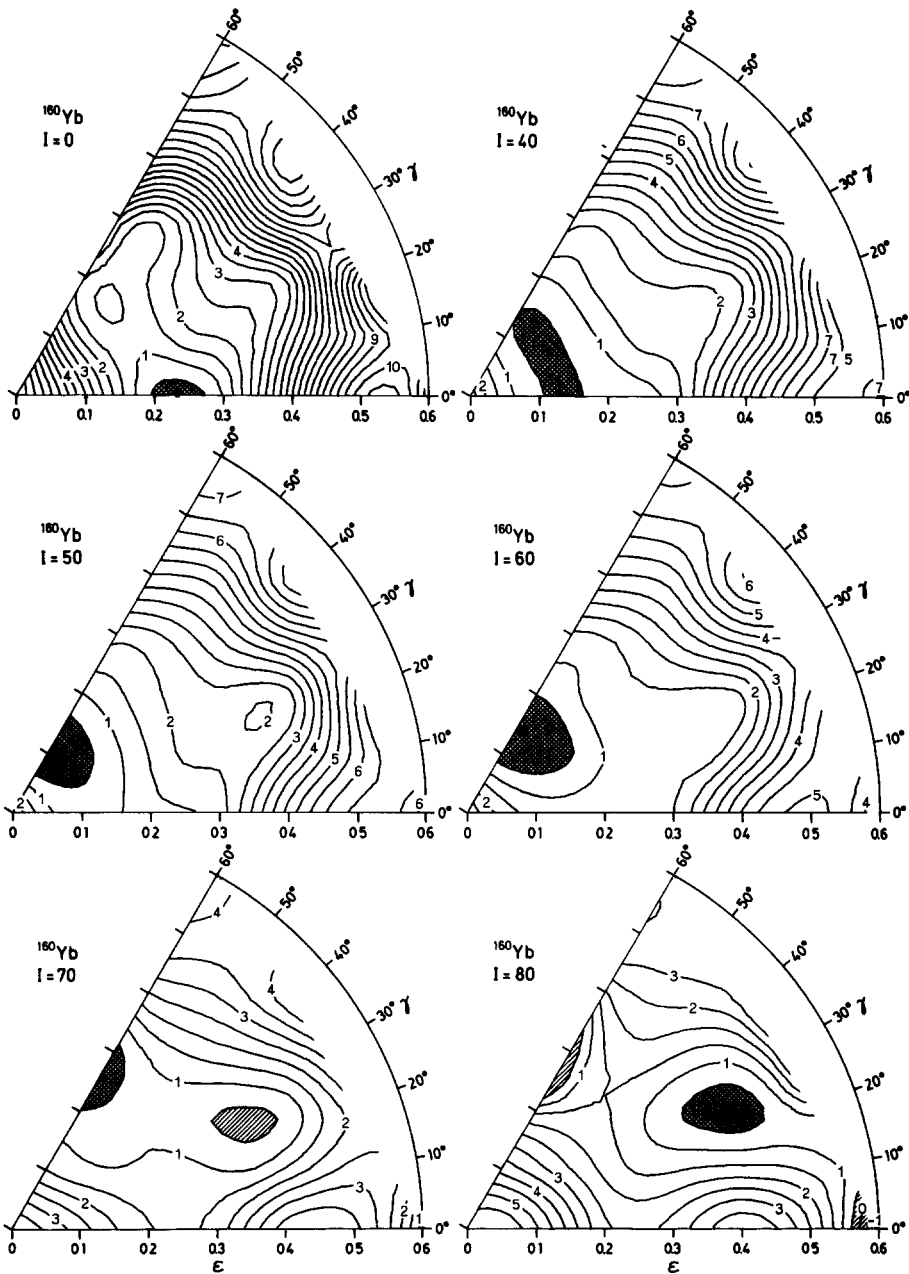
Fig 15 Potential-energy surfaces in the (ε, γ) plane with inclusion of the shell energy for ^{160}Yb as a function of angular momentum For the surface, Coulomb and macroscopic-rotation energy terms a minimisation is performed with respect to ε_4
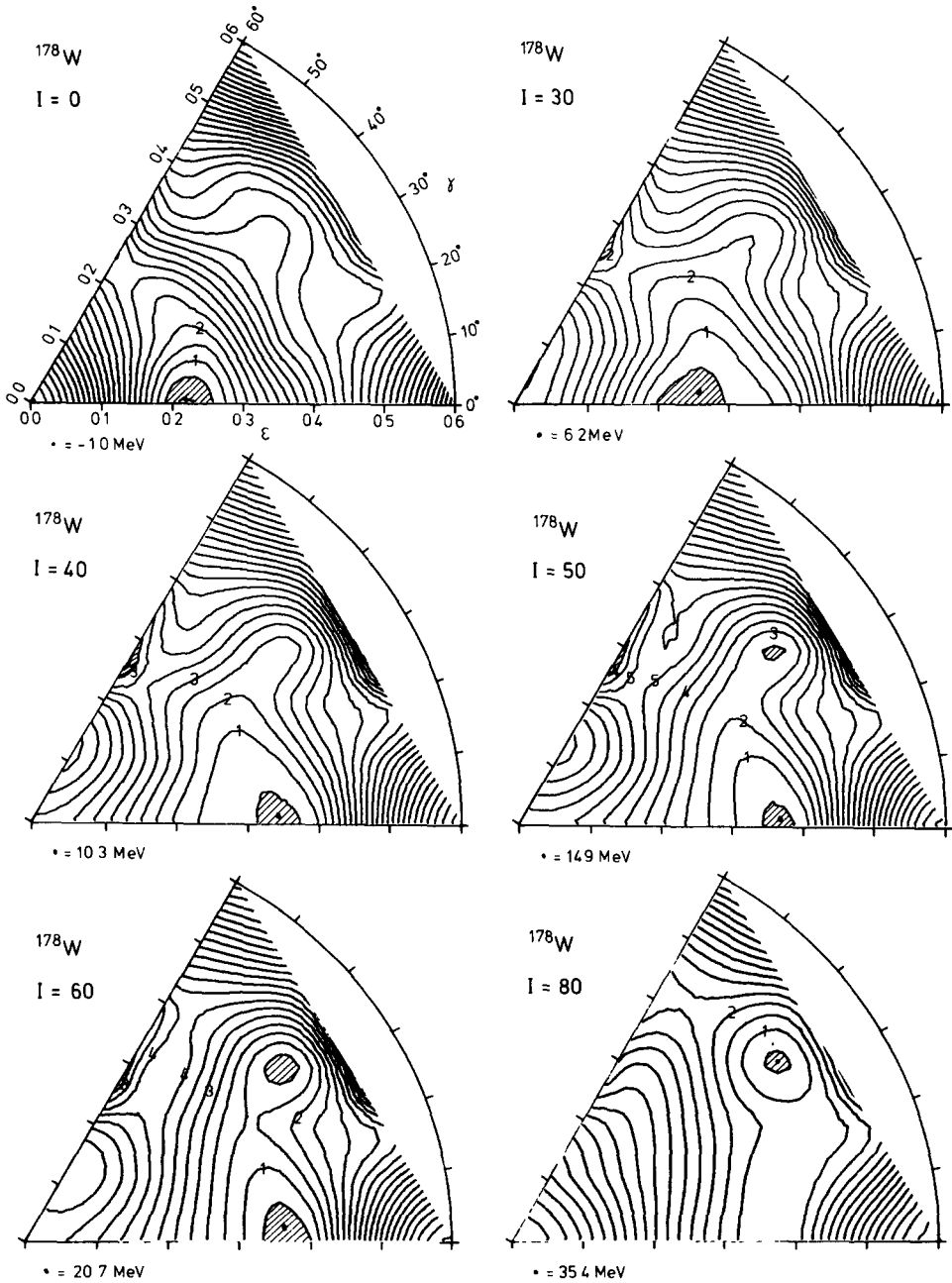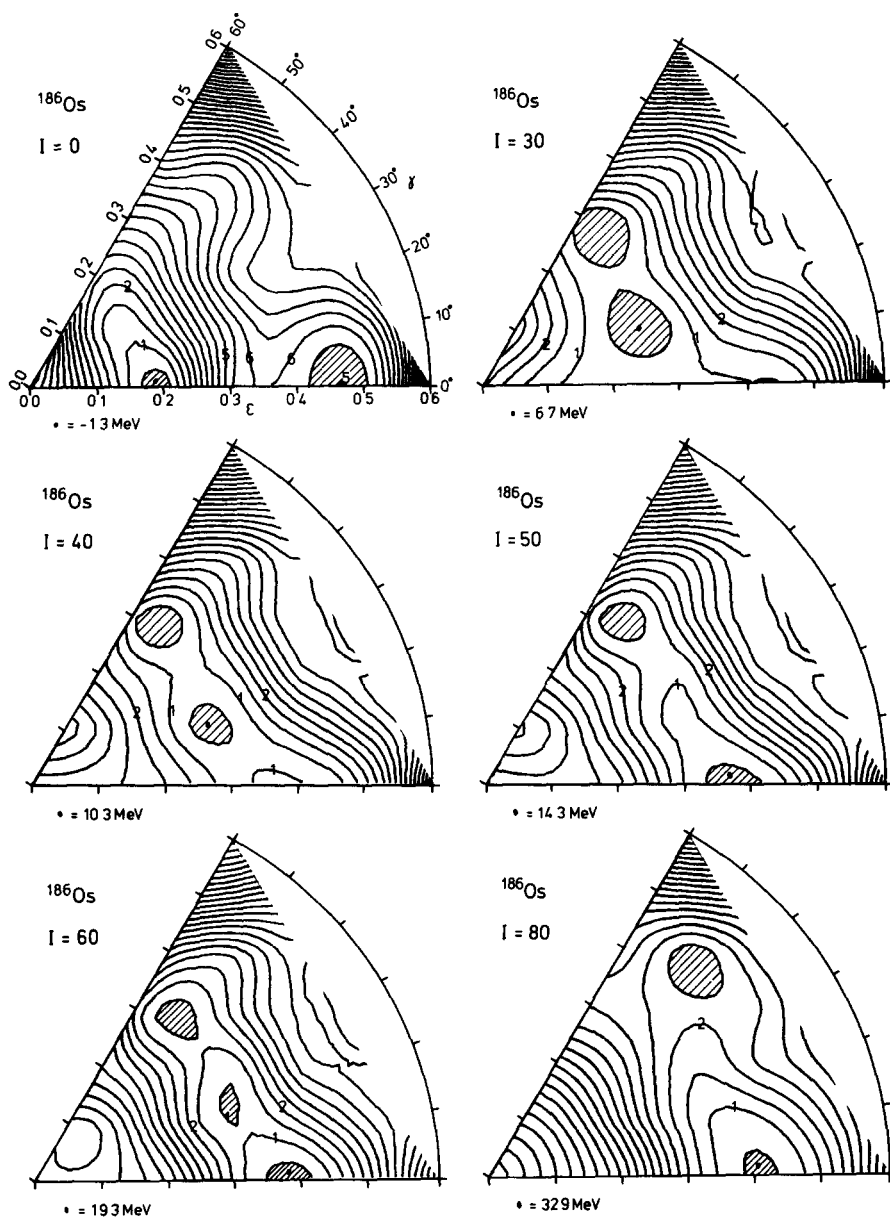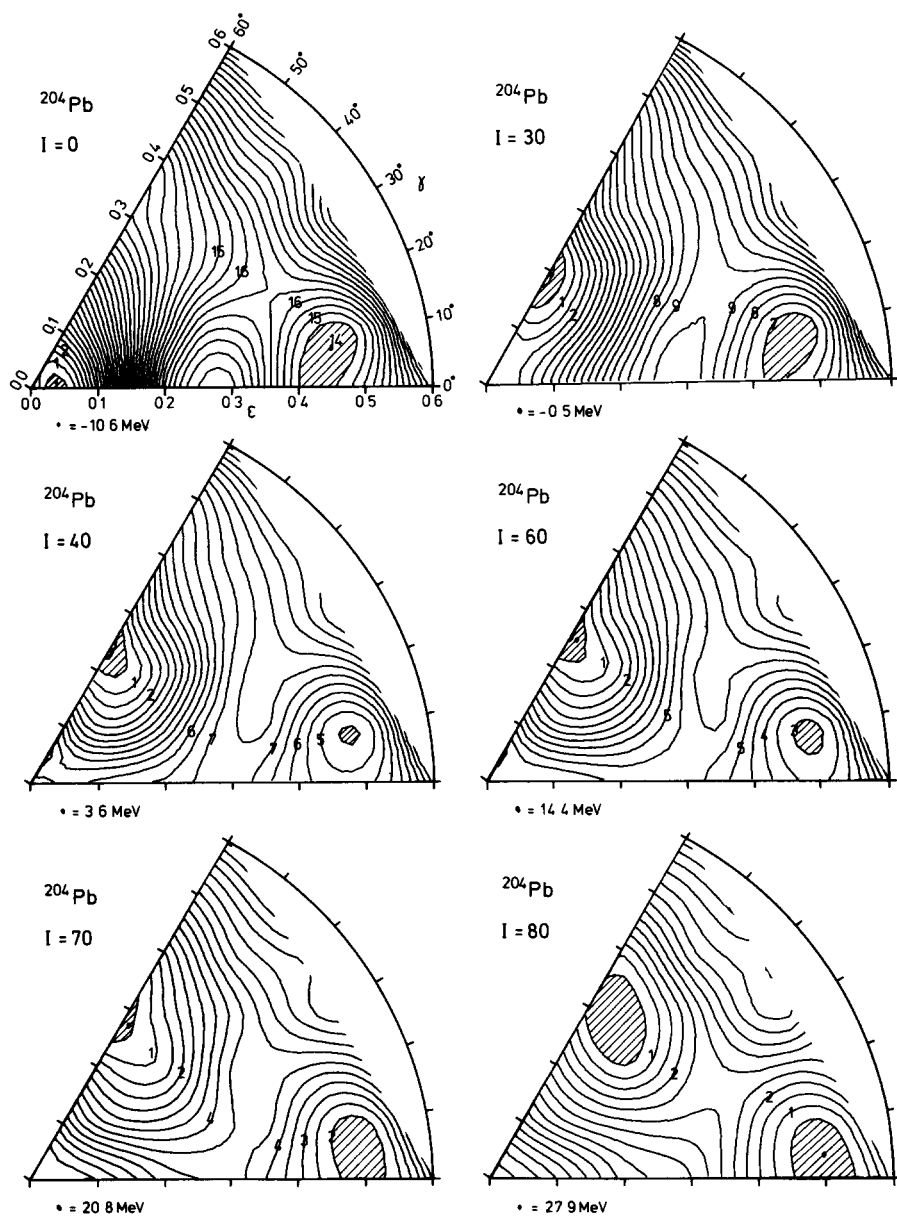
Fig 16 Same as fig 15 but for ^{178}W Energy values of the minima, as given below each plot, are measured relative to the static spherical liquid drop

Fig 17 Same as fig 16 but for ^{186}Os

Fig 18 Same as fig 16 but for ^{204}Pb

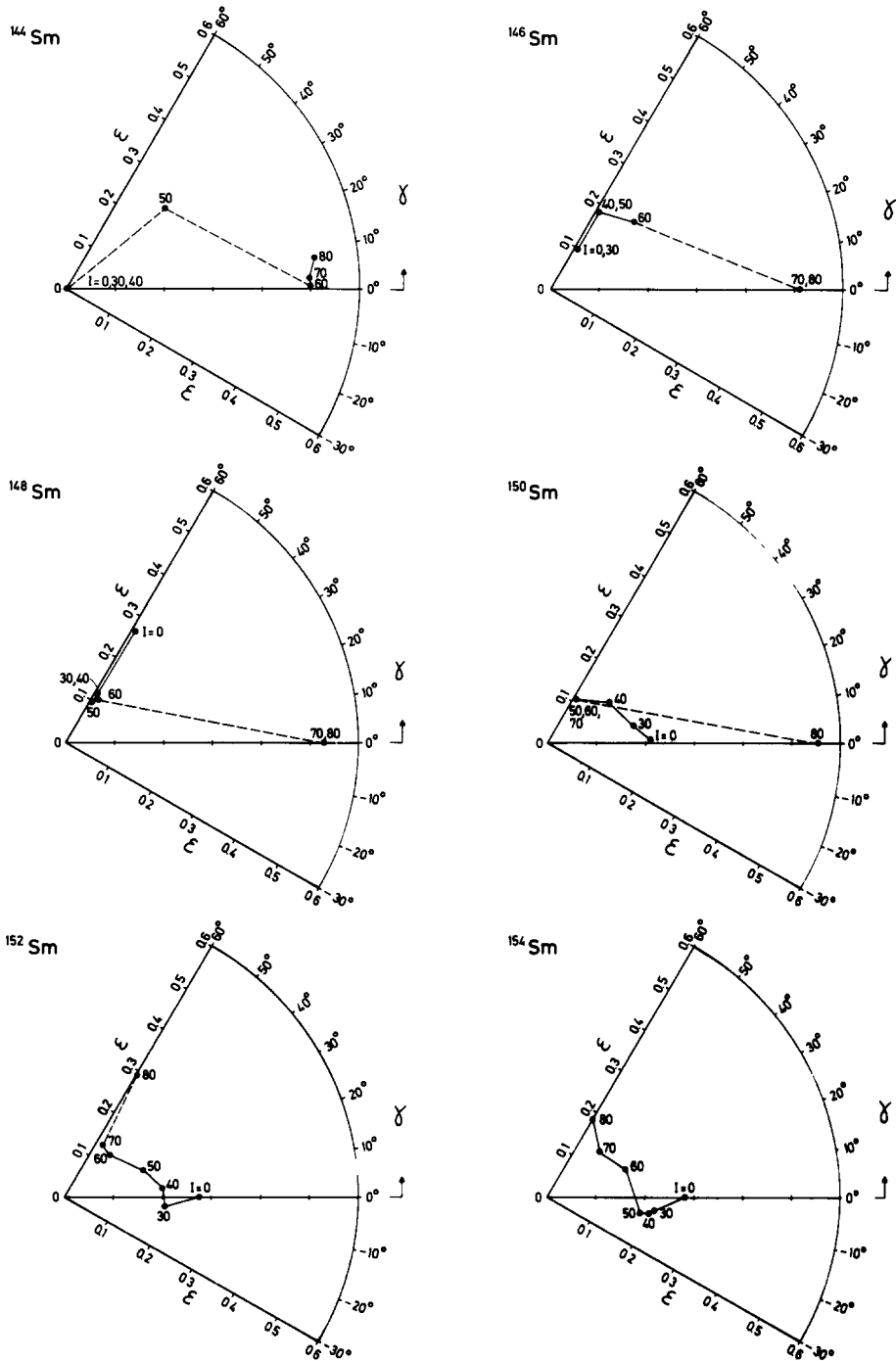Fig 19 Trajectories in the (ε, γ) plane of the minimum equilibrium shape for isotopes of Sm as a functio of total angular momentum I A continuous shift in the position of the equilibrium points is marked b a solid line Dashed line means a "phase" transition from one shape minimum to another
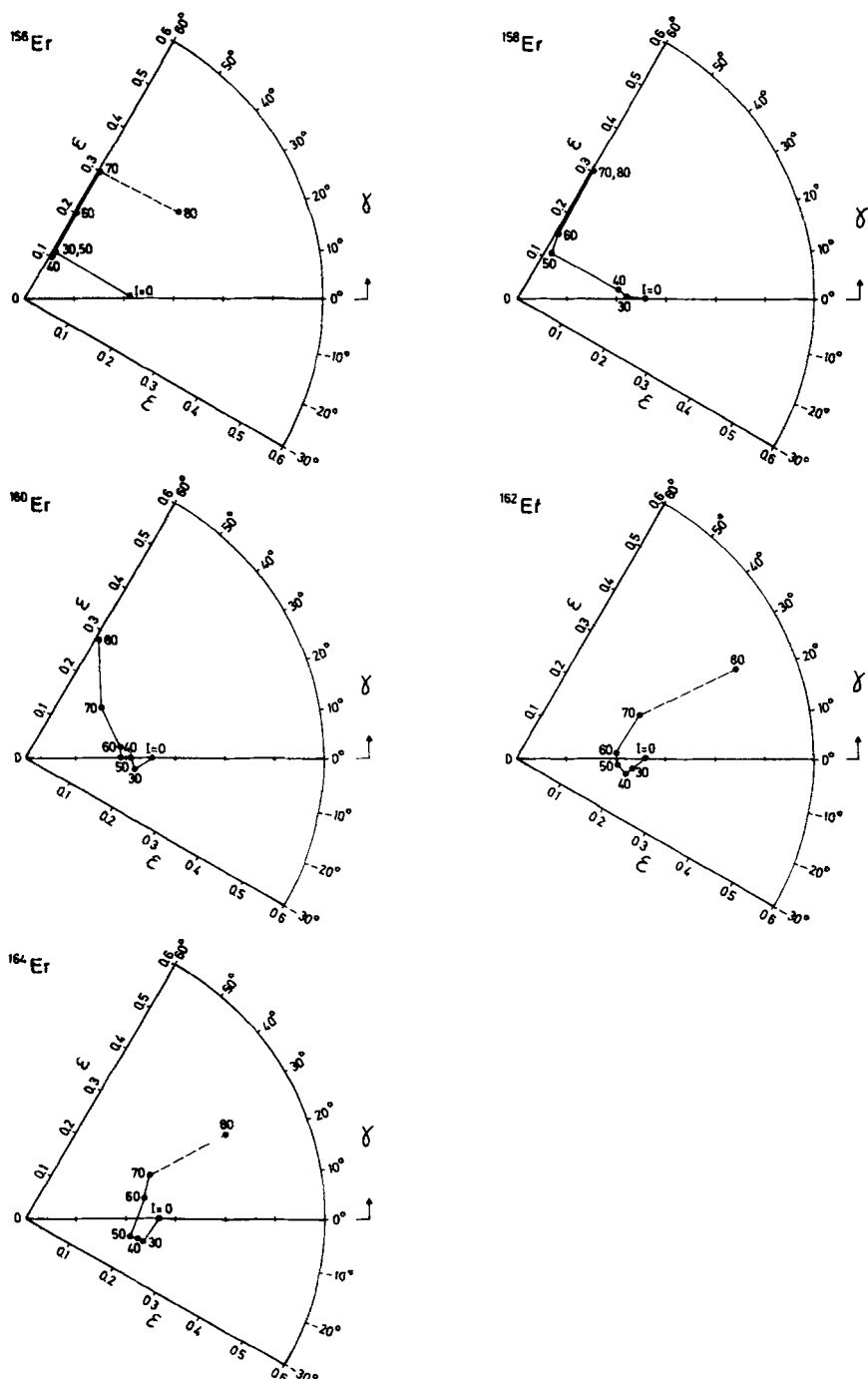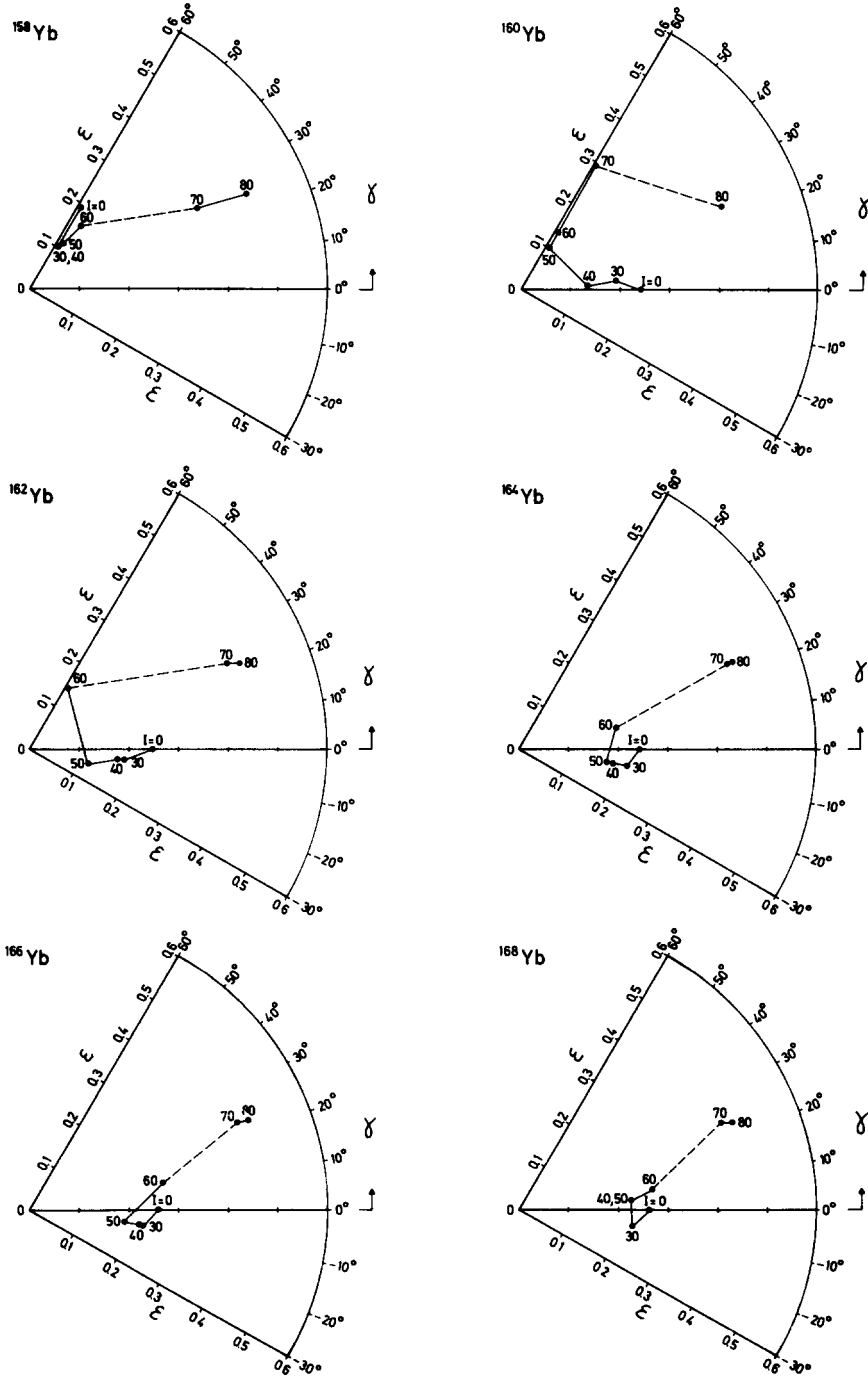
Fig 20 Same as fig 19 but for isotopes of Er

G ANDERSSON *et al*

Fig 21 Same as fig 19 but for isotopes of Yb

6 1 THE LIGHT AND HEAVY RARE EARTH REGIONS

In figs. 15–18 we give a series of potential-energy surfaces and in figs. 19–22, the trajectories indicating the position of the minimum at each spin I in the (ε, γ) plane (with implicit inclusion of ε_4 as described above) for a few interesting nuclides. Often several shapes, as one oblate, one prolate and one triaxial are competing, the absolute minimum shifting between the competing shapes as a function of I. Furthermore each minimum changes also gradually its location in the (ε, γ) plane with the change in I.

One must note that in all of the calculations pairing has been neglected. The ground state of several neutron deficient Sm, Gd nuclei, known experimentally to be
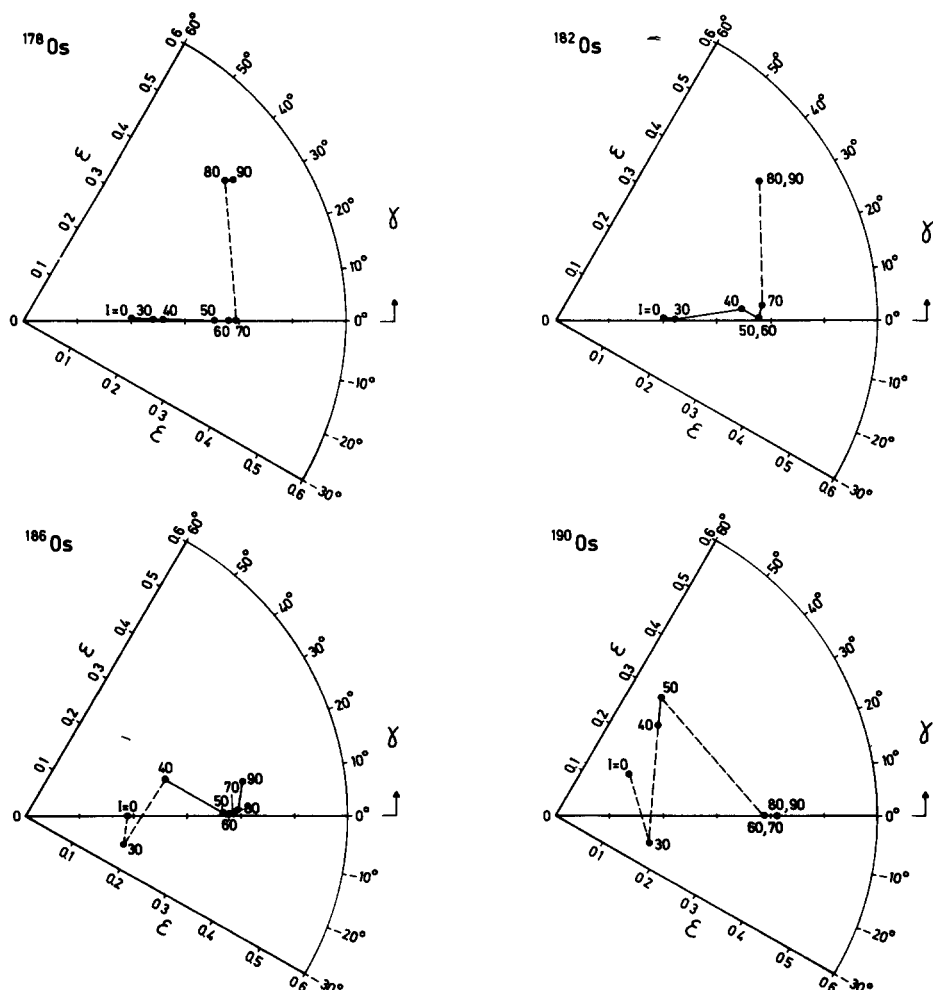
Fig 22 Same as fig 19 but for isotopes of Os

essentially spherical, are therefore generally somewhat deformed (often oblate in the calculations). For $I \geqq 30$ the used approximation of collapsed pairing should be applicable.

One typical feature of some of the light rare earth nuclei is the fact that the
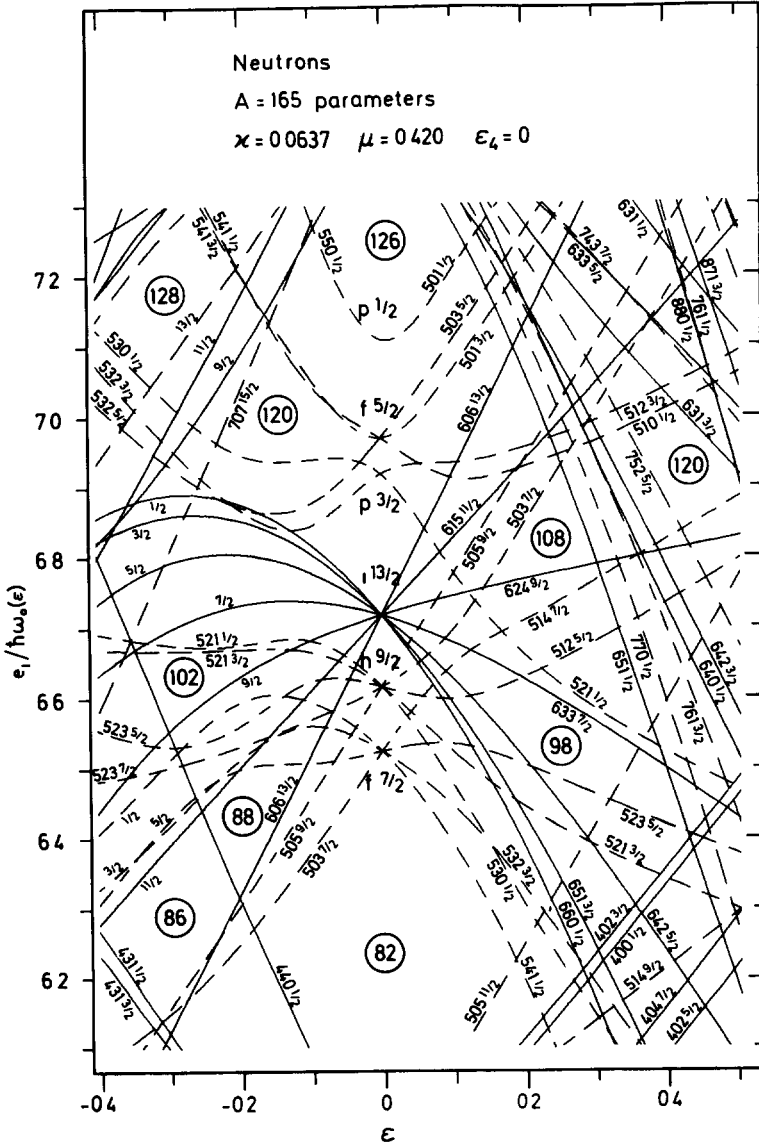
Fig 23 Single-neutron diagram for neutron numbers between $N = 82$ and 126 Note the strongly down-sloping orbitals filled for the $I = 0$ case for the oblate deformation $\varepsilon = -0 3$ The breaking of the filled pairs of these orbitals and the subsequent promotion of nucleons into above-lying orbitals is the reason for the contraction with I in ε

ground-state distortion, whether oblate as in $^{148}Sm_{86}$, $^{150}Gd_{86}$, or prolate as in $^{150-154}Sm_{88-92}$, $^{152-158}Gd_{88-94}$, $^{156-162}Dy_{90-96}$, $^{158-164}Er_{90-96}$ and $^{160-166}Yb_{90-96}$ appears to contract in $|\varepsilon|$ with increasing I

The reason for the diminishment in $|\varepsilon|$ can be directly understood from an inspection of fig. 23 exhibiting neutron orbitals as functions of ε around $N = 82$. Consider first the oblate case of $N = 88$, $\varepsilon \approx -0.2$. For this distortion the three lowest orbitals of the shells above $N = 82$ are filled pairwise for $I = 0$. The breaking of the pairs, e.g. in the orbitals $[606\frac{13}{2}]$, $[505\frac{9}{2}]$, etc., and the promotion of particles to higher orbitals leads to the generation of angular momentum The promoted particles are then placed in orbitals above the mentioned ones, which latter are less deformation driving The result is a less oblately deformed nucleus for higher I-values than for $I = 0$ The situation on the prolate side is completely similar to that on the oblate side.

For the heavy rare earths with $N \geqq 100$ the opposite effect is noticeable. Thus for $^{172-176}Hf_{100-104}$, $^{174-178}W_{100-104}$, $^{178-186}Os_{102-110}$ the effect of stretching is very apparent. In particular is ^{178}Os a good case (similar to ^{178}W, shown in fig. 16). Here for $I = 0$ the prolate equilibrium shape corresponds to $\varepsilon = 0.2$ while for $I = 70$ we find that ε has gradually increased to $\varepsilon = 0.4$. The effect is easily understood. Here the hole states are weakly stabilizing while the originally empty states originating from the next higher N-shell, occupied by the promoted particles in order to generate higher angular momentum, are strongly deformation driving. For the isotopes of Pt and Hg there is a trend to go oblate with increasing I (as is the case for the liquid drop). For the isotopes of Pb there is a trajectory from purely spherical shape out along the axis $\gamma = 60°$. Very high spin states $I \approx 70-90$ of the Pt, Hg and Pb isotopes suddenly change shape and tend to find a minimum for pure prolate shape near $\varepsilon = 0.5$. This is a competing second minimum for all spin values considered for all the studied isotopes of Pt, Os and Pb.

A few words should be added about the trend to evolve shapes with negative [†] γ as encountered for isotopes of Sm to Yb with N-values from 90 to 98. The spins involved are in the region 0–50, the ε-values from 0.2 to 0.3 and $\gamma = 0°$ to $-15°$

The negative γ-values imply that the lowest energy is reached for rotation around the medium long axis. This non-classical behaviour is caused essentially by the $N = 6$ neutrons (from the $i_{\frac{13}{2}}$ shell) which for neutron numbers $90 \leqq N \leqq 100$ are being gradually filled. Since the negative γ-deformations are small, the shape of the nucleus is predominantly prolate. However, the levels are not very well described by the prolate labelling $[Nn_z\Lambda\Omega] = [660\frac{1}{2}]$, $[651\frac{3}{2}]$, etc. Even for moderately large ω-values, as seen from fig. 24, the angular momenta of these orbitals are instead aligned along the rotation axis, i.e along the x-axis. From fig. 24 it is also evident that the alignment is almost as good for $\gamma < 0$ as for $\gamma > 0$ Thus, in an approximate treatment it should be enough to study the preference as to positive or negative

[†] The effect of negative γ-values was first observed by the authors of ref [6])

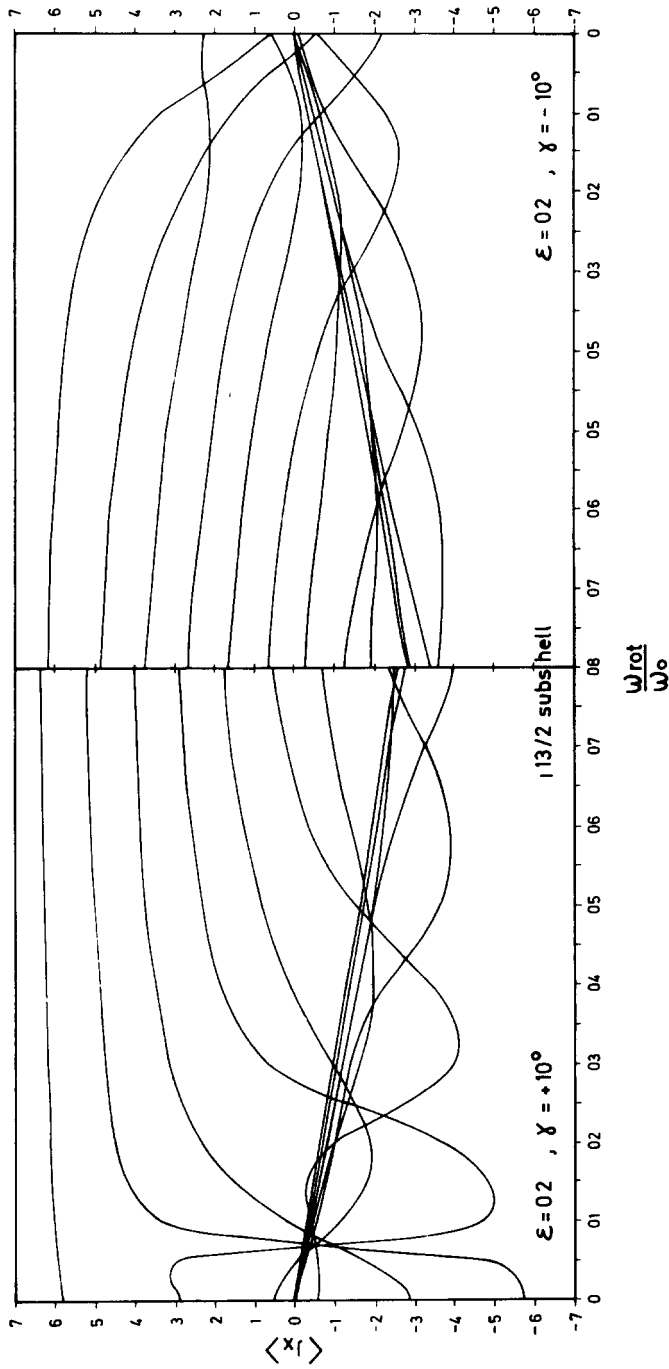Fig 24 Angular-momentum projections $\langle J_x \rangle$ of $i_{13/2}$ subshell orbitals for $\varepsilon = 0\,2$ and $\gamma = +10°$ and $-10°$, respectively Note the faster alignment for positive γ For large enough ω-values the angular momentum carried is very similar for positive and negative γ-values The upper levels (at high ω) in the figure are filled first

γ-values of the energy of different single-particle levels. For all the levels of fig. 24 it turns out that the mixture of states having $j \neq \frac{13}{2}$ is less than 10 %. One may then approximately describe them as $[N = 6, l = 6, j = \frac{13}{2}, j_x]$ where the states having $J_x = \frac{13}{2}, \frac{11}{2}, \frac{9}{2}$, etc. corresponds to the lowest values of e_i^ω, i.e. are being filled first. Actually, for $\omega = 0.06\mathring{\omega}_0$ these orbitals occur with squared amplitudes of 84, 72 and 51 % respectively.

We are now ready to consider the preference as to positive or negative γ-distortions. The perturbation term is proportional to $\varepsilon(\sin \gamma)\rho^2(Y_{22} + Y_{2-2})$. The expectation value of the latter expression for the "limiting" wave functions in question is proportional to $(3j_x^2 - j(j+1))$. For the wave functions having $j_x > 0$ this quantity equals 78, 42, 12, -12, -30, -42 and -48, respectively. Thus in this limiting case $\gamma > 0$
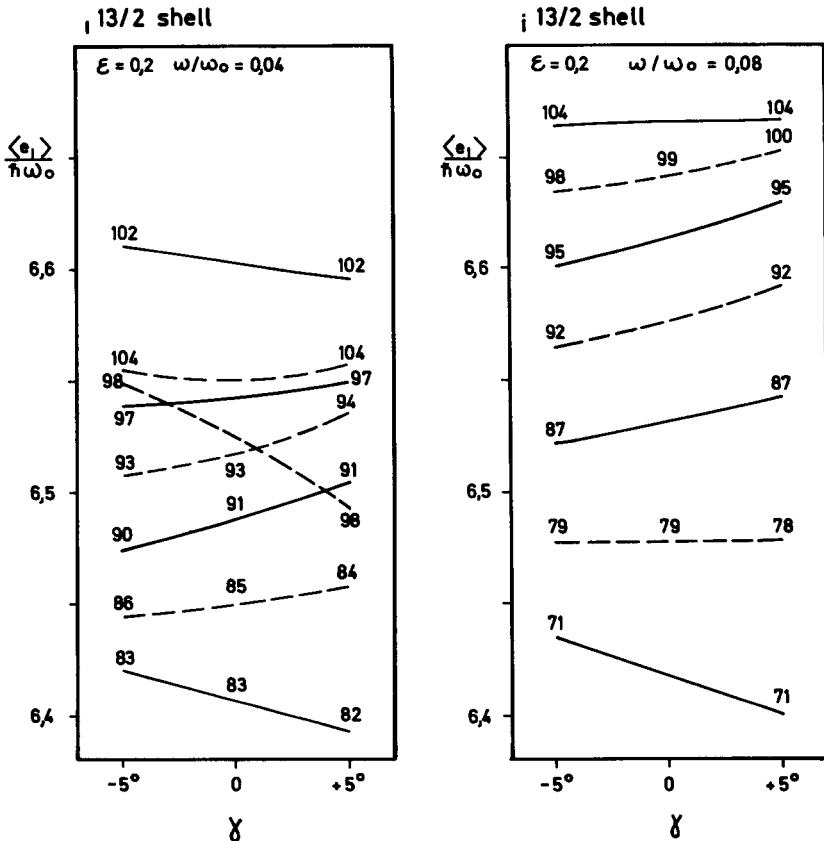
Fig 25 Single-neutron orbital energies $\langle e_i \rangle$ belonging to the $1_{13/2}$ subshell in units of $\hbar\omega_0$ as function of γ for $\varepsilon = 0\ 2$ and a rotation frequency $\omega/\mathring{\omega}_0$ of 0 04 and 0 08 The order of filling is marked by the neutron numbers listed for $\gamma = -5°, 0°$ and $5°$, respectively. While for low neutron numbers a positive γ is favoured, for $N > 92$ it appears that with the indicated levels populated negative γ values are favoured The $N = 98$ orbital gives at $\omega/\mathring{\omega}_0 = 0\ 04$ a lower energy contribution for positive γ From fig 24 it is seen that it also gives a much lower spin contribution for positive γ The higher energy at negative γ is more than compensated by the much larger spin values

is clearly favoured and it is first when all the seven states of positive J_x are filled that there is an equilibrium situation between positive and negative γ-values.

However, the actual wave functions are not so completely aligned along the rotation axes, and show up for smaller ω a systematic admixture of lower J_x components Thus, for these wave functions and for $\omega = 0.06\omega_0$ the perturbation matrix element considered above are instead 50, 8, -14, -29 etc For $\omega = 0\,06\omega_0$ and for $\gamma = 0°$ the corresponding $\langle J_x \rangle$ values are 6 2, 4.9, 3.6 and 2.2 (cf. fig 24) As for large J_x values the non-diagonal contributions from the perturbation term are rather small, it is reasonable to insert these $\langle J_x \rangle$ values in the above asymptotic formula. We then get the numbers 66, 22, -13 and -34 in rather close agreement with the exact results If the numbers are added it is evident that, for $\omega = 0.06\tilde{\omega}_0$, only five particles are needed in the $N = 6$ shell to give a driving force towards negative γ-values However, for smaller ω-values the $\langle J_x \rangle$ values are smaller (fig. 24) and thus fewer particles are needed in the $N = 6$ shell to give negative γ-values This explains why for $I = 30$ ($\omega = 0\,03$–$0\,04$) negative γ-values are observed already for neutron numbers $N = 90$, i e for three particles in the $N = 6$ shell On the other hand for $\omega = 0\,07$–$0\,08\,\tilde{\omega}_0$, i e for spin values around $60\hbar$ it is just the nuclei with $N \geq 96$ that show negative γ-values. Of great importance are also second-order effects i.e. the mutual repulsion of the subshell levels, which are closer on the $\gamma < 0$ side This provides some additional effect to force the nucleus towards negative γ-values

For small ω-values (up to 0.01–$0\,04$ depending on the neutron number) the preference for $\gamma < 0$ is mainly determined by the fact that when the first state of the $11\tfrac{3}{2}$ subshell becomes aligned with the x-axis, also states with large negative $\langle J_x \rangle$ values compete for $\gamma > 0$ As long as these states are filled $\sum\langle J_x \rangle$ is always smaller for $\gamma > 0$ than for $\gamma < 0$. However, $\sum \langle e_i \rangle$ depends only weakly on γ, since the states with the lowest possible $\langle e_i \rangle$ are filled for all γ-values, cf. fig 25. Thus $\gamma < 0$ is favoured, since an increase of the angular momentum at constant energy lowers the yrast line.

It must however be recognized, that the energies $\langle e_i \rangle$ are mainly determined by the orientation of the orbitals, with respect to the longest axis (i e for the pure prolate shape the symmetry axis) Therefore an alternative way of comparing positive and negative γ-values is to correlate the expectation value of J_z, where z corresponds to the symmetry axis for the prolate nucleus, to the energies $\langle e_i \rangle$. It turns out that these two quantities are almost proportional. A small value of $\langle J_z \rangle$ corresponds to more quantal nodes in the z-direction, i.e. to a lower energy. As a consequence of the large negative $\langle J_x \rangle$ states for $\gamma > 0$, which exploit much of the low J_z components, it turns out that for positive γ the $\langle |J_z| \rangle$ of the aligned (and filled) states are larger and thus more quanta have been transferred from the z to the perpendicular direction This transfer of quanta will however cost energy and thus the negative γ-values are preferred within a certain limit of spins and particle numbers

It should also be mentioned that the negative γ-values described above are not only a neutron effect The $h_{\frac{11}{2}}$ protons which can be treated analogously to the $11\tfrac{3}{2}$
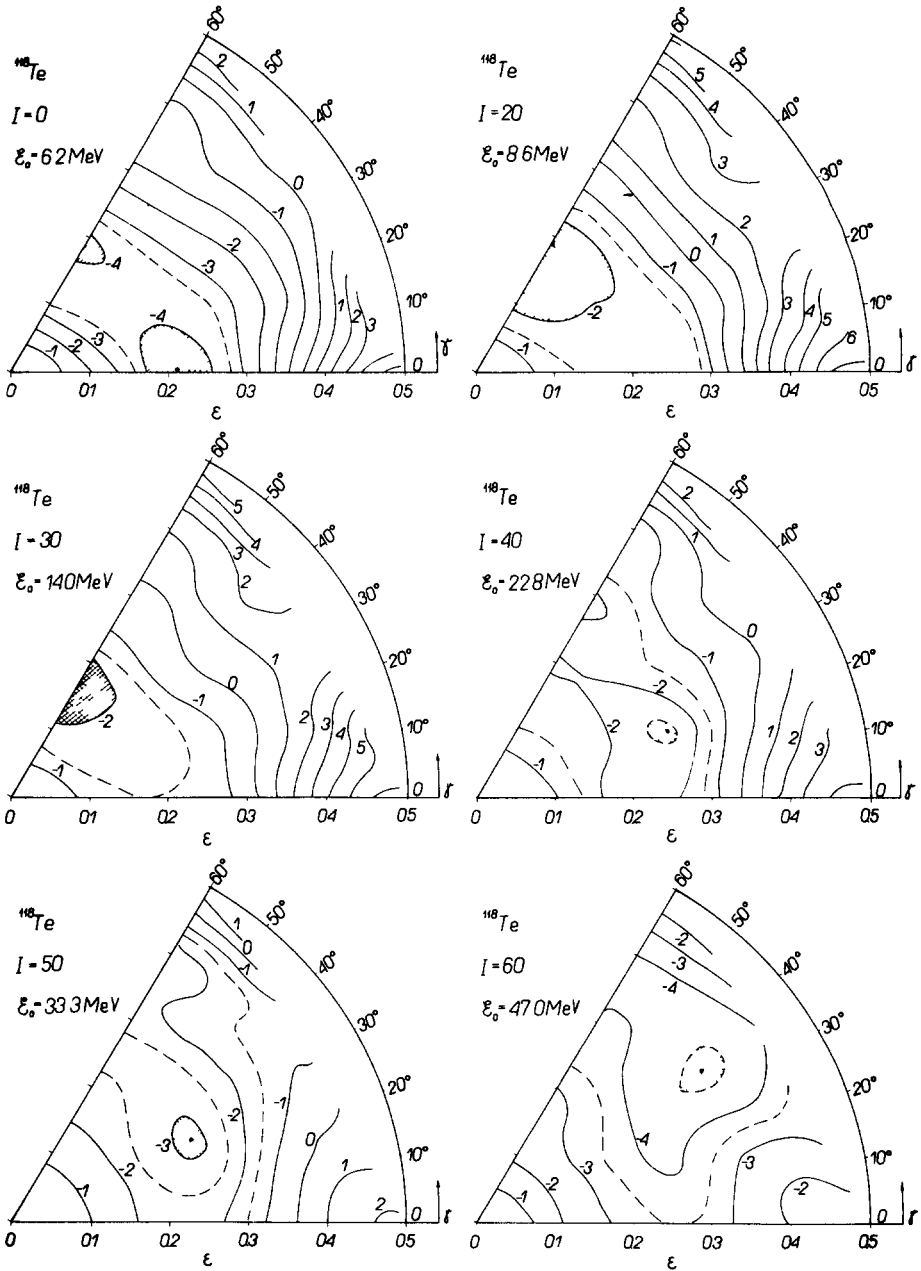
Fig 26 Potential-energy surfaces with shell energy included for a series of I-values for the nucleus ^{118}Te
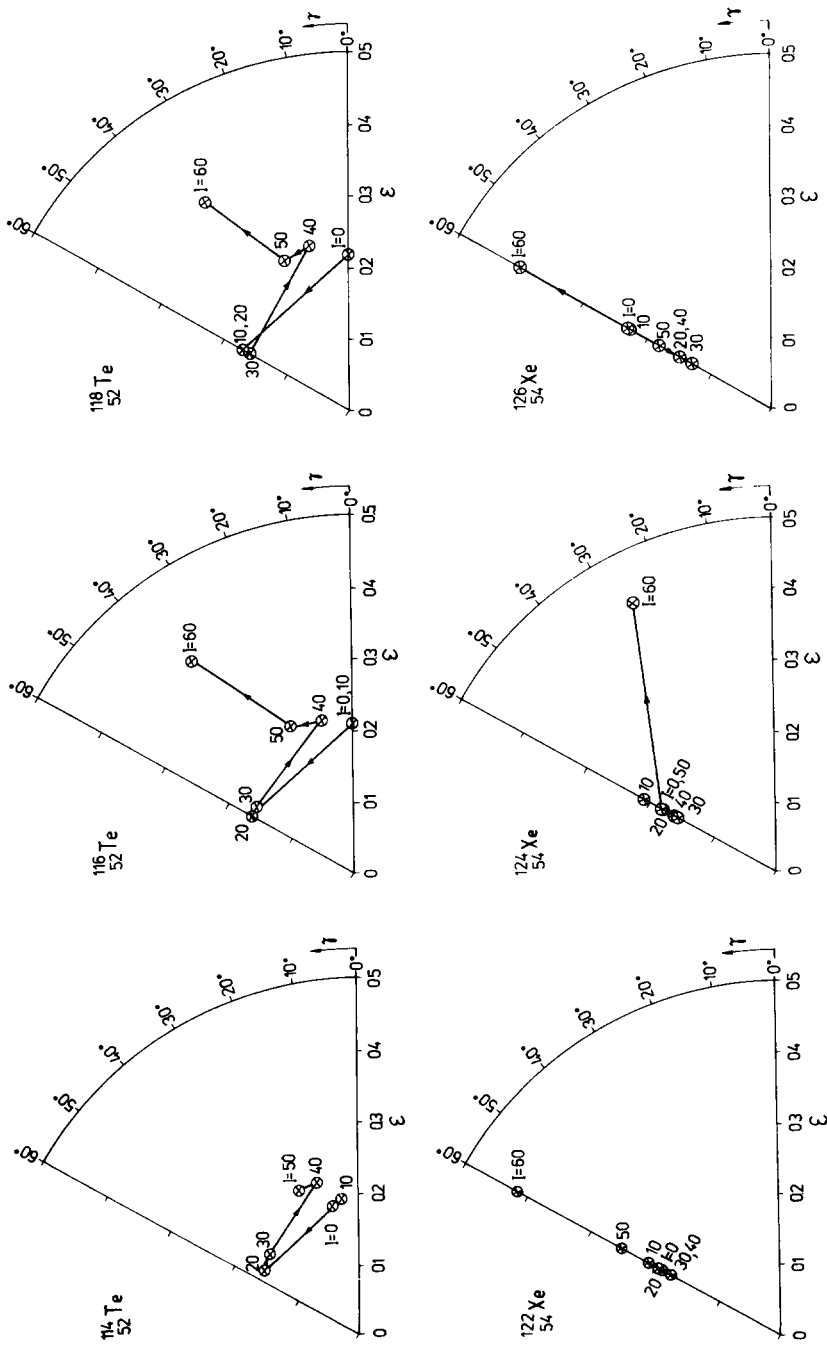
Fig 27 Equilibrium shape trajectories for isotopes of Te and Xe
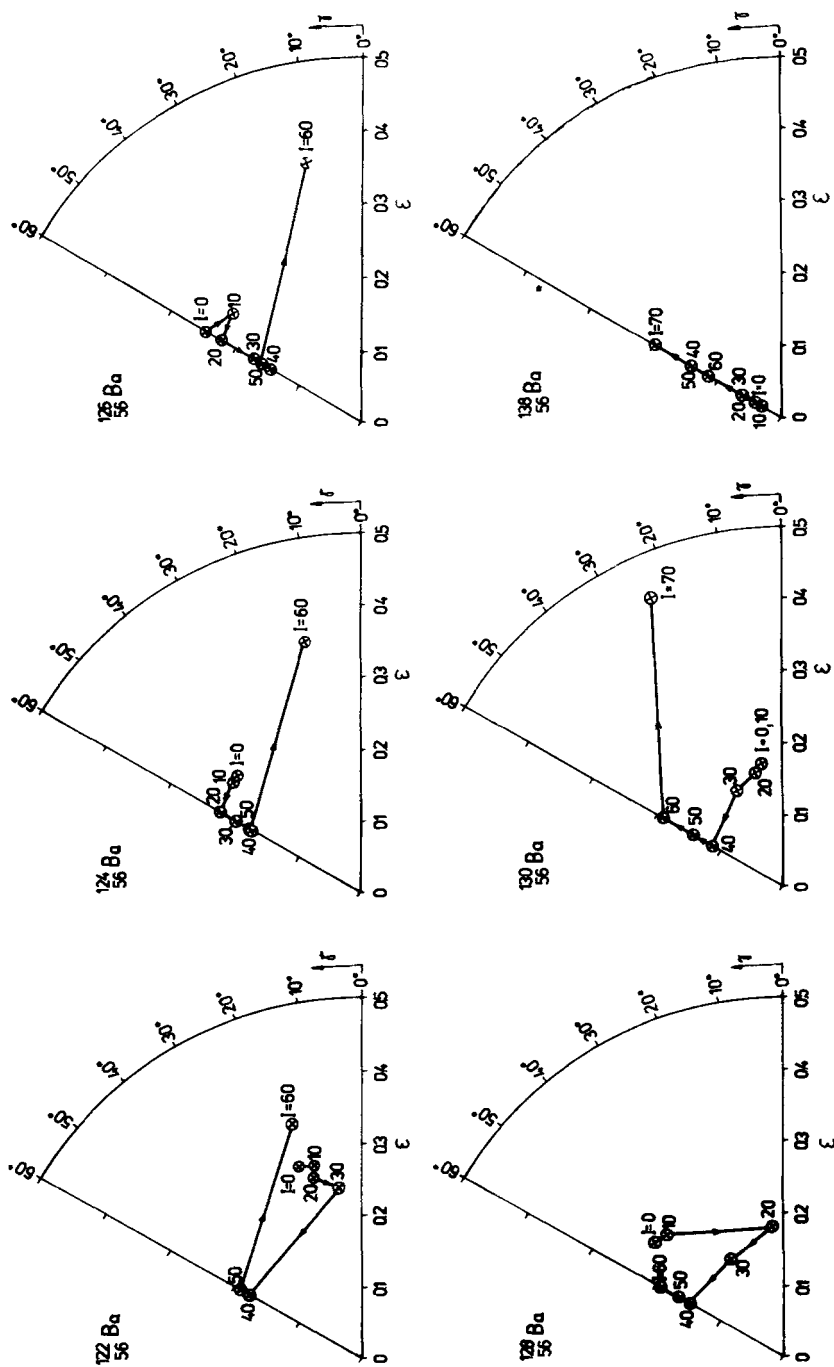
Fig 28 Equilibrium shape trajectories for isotopes of Ba
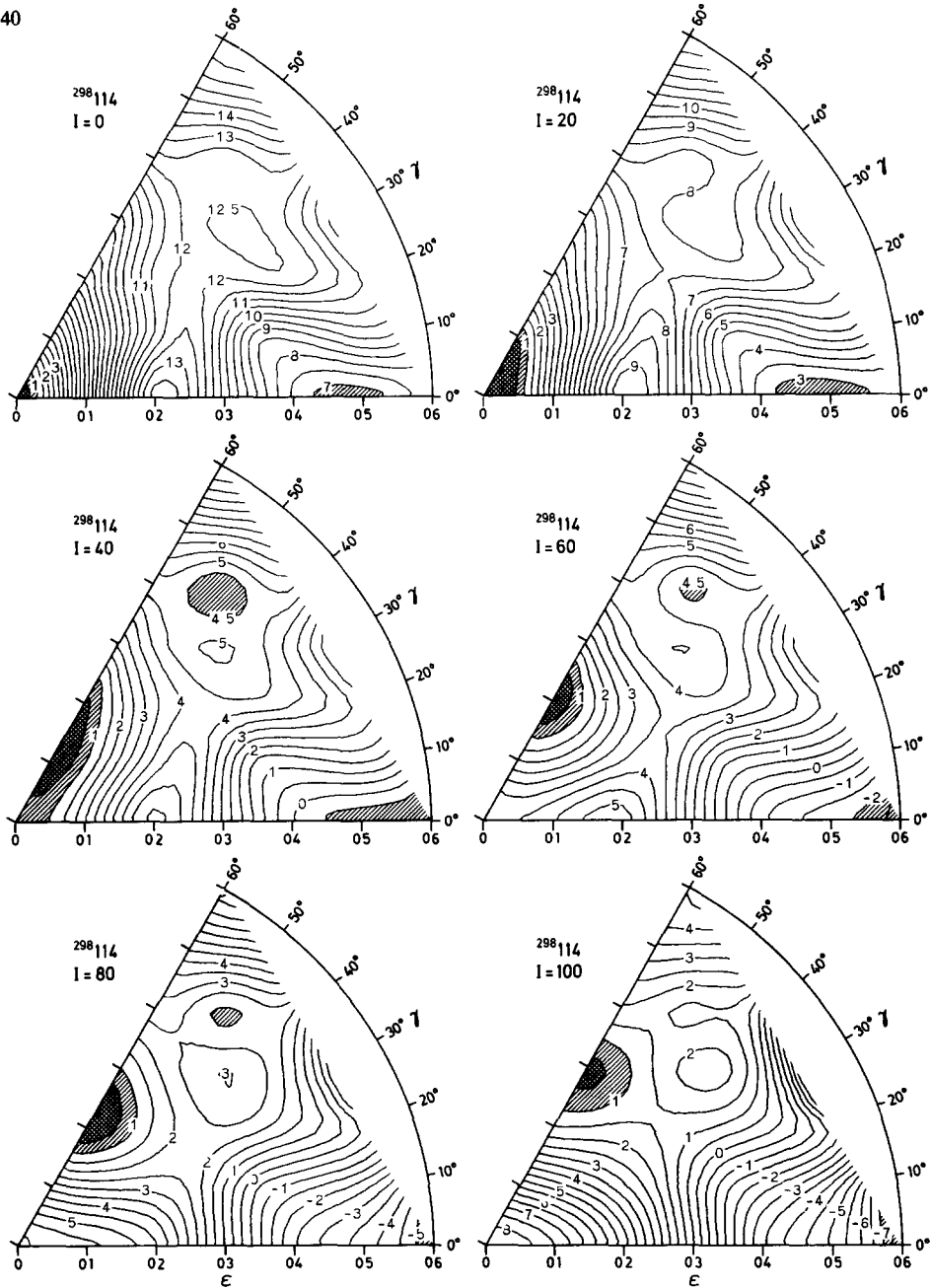
Fig 29 Same as fig 27 for the super-heavy nucleus $^{298}114$ The change in shape ("flattening oblates") is similar to that encountered for ^{208}Pb and ^{204}Pb (shown) The macroscopic and shell energy variations with I cooperate and are responsible for the persistence of a barrier towards fission even at very high spin values The barrier towards fission for the oblate minimum thus remains when the barrier along the prolate axis has long since vanished This feature of a remaining stability towards fission is a so far highly unexpected feature that appears very favourable for the prospect of super-heavy element production

neutrons have a similar but smaller influence. Additionally, in other regions with a few particles in high-j intruder shells, similar effects might also be expected.

6 2 THE Te–Ba REGION

Fig 26 illustrates the potential-energy surfaces in the ^{118}Te nucleus for various values of I from 0 to 60. The neutron deficient isotopes in this region are known as typical examples of the γ-soft nuclei at low angular momentum The same property seems to show up for angular momenta increasing up to $I = 30$, this is all under the assumption that the pairing force does not alter the picture. For $I = 40$ a triaxial equilibrium shape seems to prevail, and for $I = 60$ the minimum is shifted towards larger elongations.

The resulting trajectories that characterize the minima in the potential-energy surfaces are shown in fig 27 for some Te and Xe nuclides, and in fig. 28 for Ba nuclides The Te isotopes are seen to be very soft with respect to γ-deformation in the region of low angular momenta. The Xe isotopes exhibit mostly oblate shapes showing a slight contraction in $|\varepsilon|$ at I below 40 and then a considerable stretching at higher angular momenta. Similarly, the light Ba isotopes exhibit some contraction in deformation at lower angular momenta, while the neutron rich nucleide ^{138}Ba shows a considerable stretching (at $\gamma = 60°$) on the average.
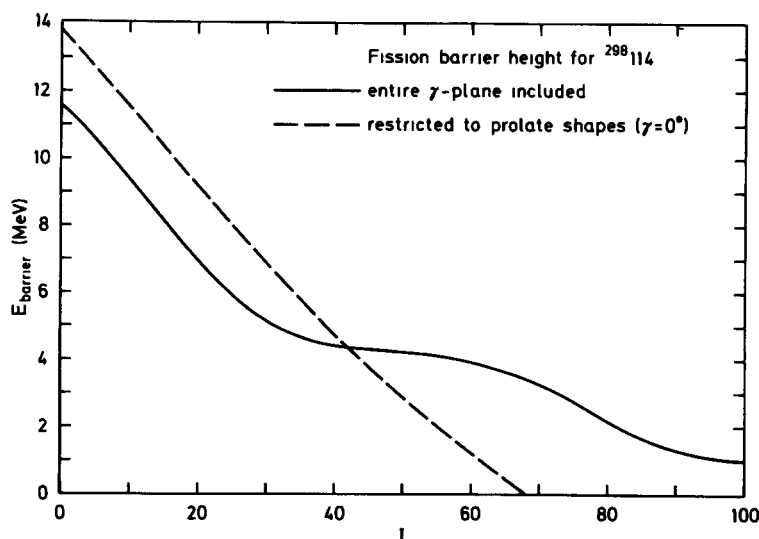
Fig 30 The calculated fission barrier as a function of I for the nucleus $^{298}114$, for two alternative cases In the case marked by the dashed curve the effect of γ-distortions is neglected In the case marked by the solid curve the effects of γ-distortions both on the minimum and the barrier are properly included For $I > 40$ the barrier height is increased when the entire (ε, γ) plane is included

6 3 THE Ne–Mg REGION

The experiences from the calculations in the rare-earth region are grossly repeated in the light deformed region. Thus in the beginning of the (s, d) shell there is a tendency to contract in deformation with increasing I, for low I-values, and to stretch at the end of the (s, d) shell. The conclusion drawn from these calculations which will appear in a forthcoming publication [16]) is that the equilibrium shape gradually changes from deformed prolate to oblate. In this regime of mass it is generally assumed that there is no pair correlation. Our results should therefore be applicable also for low spins.

6 4 THE SUPER-HEAVY ELEMENT REGION

The elements near $N = 184$ and $Z = 114$ remain surprisingly stable towards fission, as seen from fig. 29 for $^{298}114$, even at large I-values For this nucleus, even at $I = 90$ there is about 1 MeV of fission barrier. The behaviour of the equilibrium shape with angular momentum, involving a series of increasingly flattening oblate shapes, is highly similar to that of the doubly closed shell nucleus ^{208}Pb. The unexpected stability towards fission of the high angular momentum states (see fig. 30) appears to be a highly promising feature improving the prospect of an eventual synthesis of super-heavy elements

7. Wobbling motion

The discussion so far has concerned the proper yrast states. Also the states immediately above the yrast ones are of great interest, in particular in the triaxial region. The characteristic features of these states have been discussed by Bohr and Mottelson [17]) [see also refs [2, 18])] in the case of rapid rotation of a triaxial nucleus

In the present calculation the shape of the potential and the single-particle wave functions for high angular momenta have been determined. It therefore appears worthwhile to give quantitative estimates in a particular case for the parameters entering the discussion of ref. [17]) of this region. Let us recall that most of the excitation energy in the yrast region is associated with only one mode: the rotational motion. Consequently, the nucleus in the yrast region remains rather cold and, therefore, exhibits similar structure of the quantum excited states as in the low energy region, just above the ground state In case of a fast rotation of a triaxial nucleus, one may assume that in the first approximation the nucleus rotates about the fixed axis of the largest moment of inertia (say, 1-axis, then $I \approx I_1$). On top of this, the wobbling motion of the rotation axis with respect to the fixed direction of the angular momentum vector I is superimposed as a rather small perturbation. These assumptions lead to the picture of the excited levels forming channels roughly parallel to the yrast line [see also ref. [19])]. The E2 γ-transitions along each channel are strongly

enhanced while the inter-channel transitions are retarded. If $A_1 < A_2 < A_3$ denote the inertial parameters of a triaxial nucleus ($A_1 = \hbar^2/2J_1$, etc), the energy $\hbar\omega_w$ of the wobbling mode can be calculated according ref [17]) as

$$\hbar\omega_w = 2I\{(A_2-A_1)(A_3-A_1)\}^{\frac{1}{2}}.$$

The total energy in the state (n, I) is

$$E(n, I) = A_1I(I+1)+\hbar\omega_w(n+\tfrac{1}{2}),$$

where n is the quantum number corresponding to the wobbling mode.
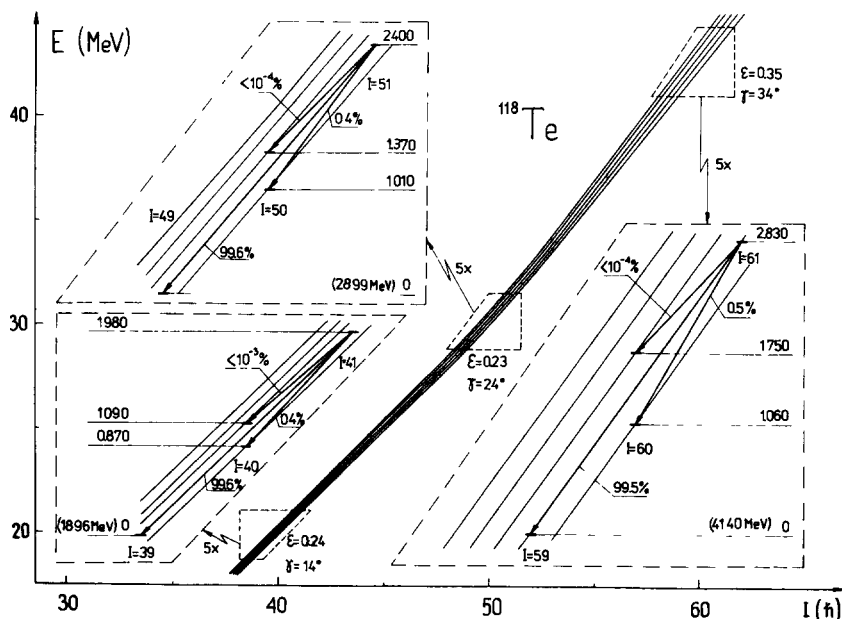
Fig 31 Theoretically calculated bands associated with the wobbling motion in the triaxial system in the region $I = 40$–60 for the nucleus ^{118}Te Note that the inter-band leaking γ-transition probability between the $n = 1$ band and the yrast band is only of the order of 0 5 % in this region of spin

TABLE 1

Wobbling motion parameters in ^{118}Te

Angular momentum	Equilibrium deformation		A_1 (MeV)	A_2 (MeV)	A_3 (MeV)	$\hbar\omega_w$ (MeV)
	ε	γ				
40	0 24	14°	0 0112	0 0117	0 0149	0 112
50	0 23	24°	0 0111	0 0120	0 0146	0 177
60	0 35	34°	0 0102	0 0118	0 0153	0 345

Having determined the nuclear shape parameters ε and γ for each angular momentum I, we can now attempt to calculate the channel spectrum and transition probabilities.

For the sake of illustration we have chosen three angular momentum states $I = 40, 50$ and 60 in the nucleus ^{118}Te and calculated the rigid body inertial parameters A_1, A_2 and A_3 for these states. The results are given in table 1.

The resulting channel structure of the spectrum in the yrast region has been illustrated in fig 31 The transition probabilities have also been calculated (we omit the details; for the formulae see ref. [17])). The results are shown in fig. 31. The channel structure of the spectrum can be clearly seen.

8. Possible yrast traps in the oblate region

Very little is known experimentally about the structure of nuclear motion, the resulting coupling scheme, moment of inertia, etc., in the oblate region at high angular momenta. In particular, it seems of special interest to examine the possibility of the existence of relatively long-lived high angular momentum states. Such a possibility was early suggested in ref. [3]). In the present investigation we attempt to gain some preliminary orientation about the regions of neutron and proton numbers, angular momenta, deformations, etc., that could characterize good candidates for a more thorough investigation of the extra-stable high angular momentum states. For this reason we are interested in the calculation of the total energy E_{tot} and shell correction E_{shell} as functions of angular momentum I for various nuclei and different oblate deformations.

As mentioned before, in case of axial symmetry in the rotating potential ($\gamma = 60°$), the nucleus forms its angular momentum I out of the individual single-particle contributions m_i. Fig. 32 illustrates the occupation of levels below the tilted Fermi surface in case of a pure harmonic oscillator. It is immediately seen that not all the values of angular momenta I can be obtained in an "optimal configuration" (i.e corresponding to a straight Fermi surface, cf. sect. 3) from summation of the individual particle contributions. If, for example, with the increasing slope of the Fermi surface one of the states (m_i, e_i) becomes occupied, while another, say (m_j, e_j) becomes empty, there is a positive discontinuity in I of the magnitude

$$\Delta I = m_i - m_j.$$

The corresponding positive jump in energy is

$$\Delta E_{s\,p} = e_i - e_j.$$

This discontinuity corresponds to the crossing of the energy levels e_i^ω and e_j^ω considered as functions of the rotation frequency ω, as was discussed before. The two quantities $E_{s\,p}$ and I then stay constant with ω increasing until a new crossing of energy levels e_i^ω occurs. The graphs of energy $E_{s\,p}$ and spin I versus ω (for $\gamma = 60°$
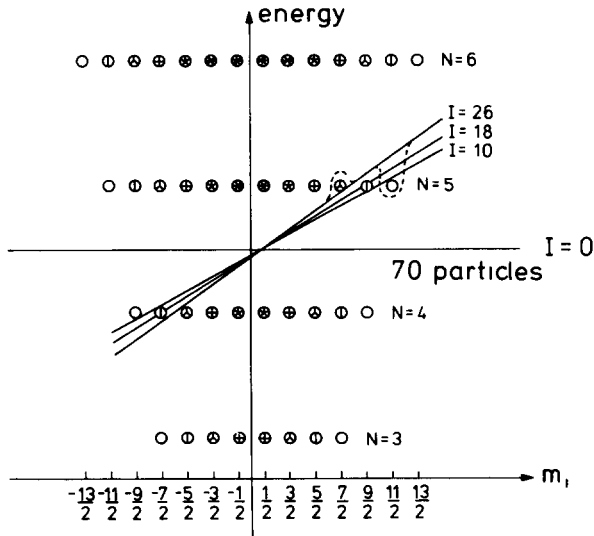
Fig 32 Single-particle energy levels e_i in the spherical harmonic-oscillator potential plotted as functions of the angular momentum projection m_i Patterns inside the circles denote the degree of degeneracy of each level Four consecutive positions of the Fermi surface corresponding to the optimal values of angular momenta $I = 0, 10, 18$ and 26 are shown The dashed lines indicate an example of the formation of the particle-hole states An $I = 24$ state is constructed on top of the $I = 26$ optimal state by creating an $m = \frac{11}{2}$ hole and placing the particle in one of the three possible $M = \frac{7}{2}$ particle states in the $N = 5$ major shell
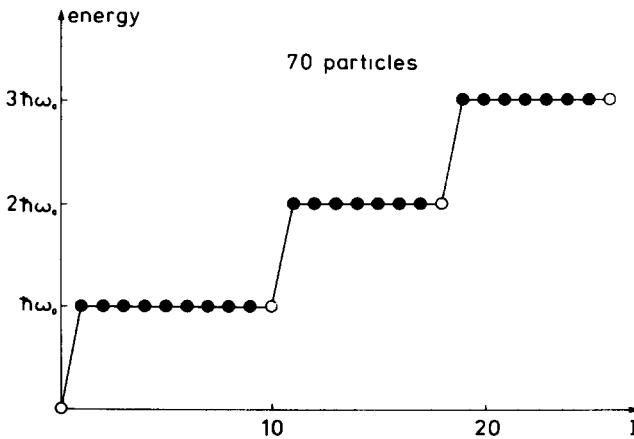

Fig 33 An yrast plot corresponding to the spherical harmonic oscillator potential Open circles denote the optimal states, while black ones denote the lowest particle-hole states
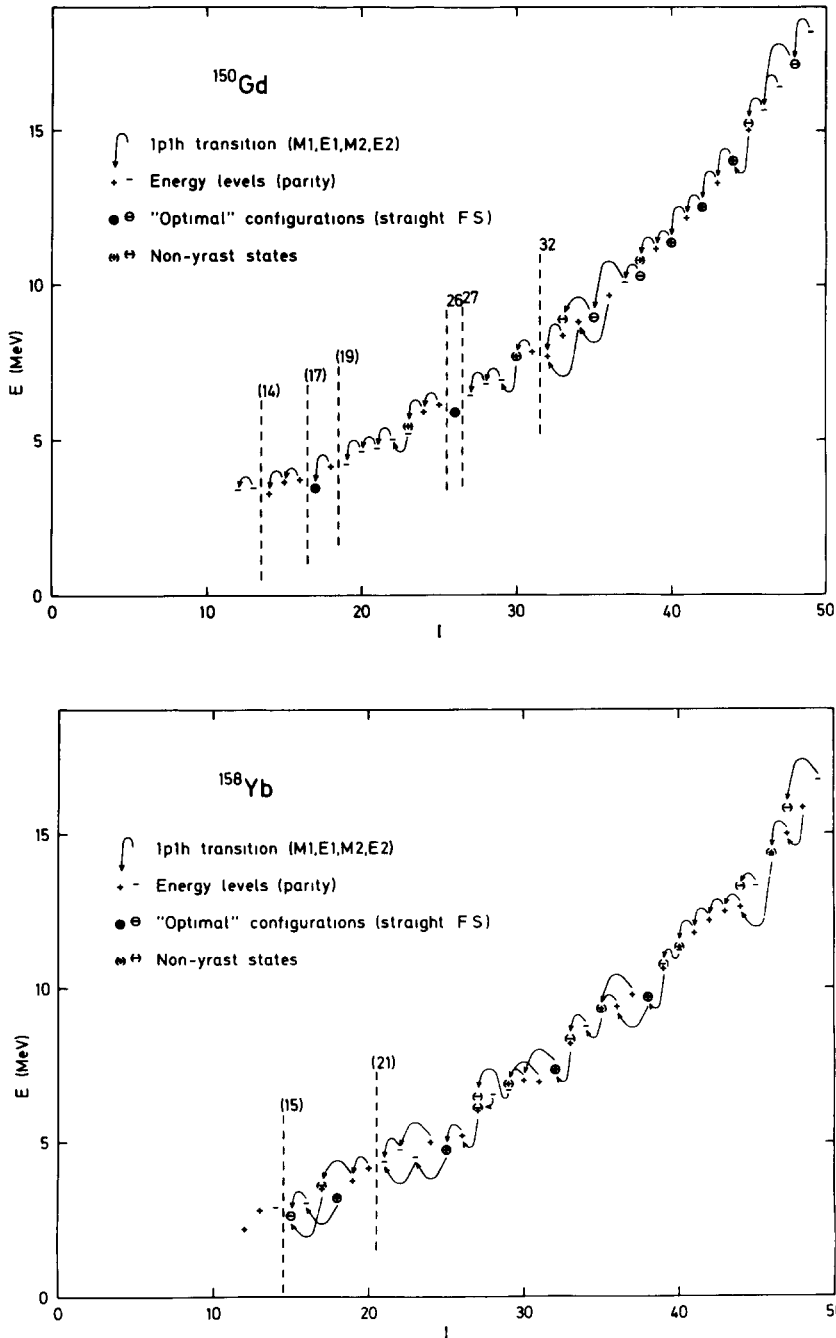
Fig 34 Theoretically calculated single-particle yrast bands for two nuclei, ^{150}Gd and ^{158}Yb, which latter nucleus according to fig 21 has a minimum-energy shape trajectory along the oblate axis in the deformation plane for $0 \leqq I \leqq 50$ Possible configurations of 1p1h and 2p2h character relative to "optimal" configurations (near equilibrium shapes) are considered They are allowed to establish minimum energy through variation in deformation ε Arrows mark possible low-multipole γ-transitions involving allowed change of configuration of 1p1h type Traps are marked by dashed line to the left of the point in question

Fig 35 Theoretical and experimental yrast band for ^{204}Pb The calculated yrast configurations are each allowed to adjust the corresponding shape Note the modest rise in E with angular momentum I, being more nearly linear in I than quadratic The energy of all spin states are calculated separately No interpolation is made
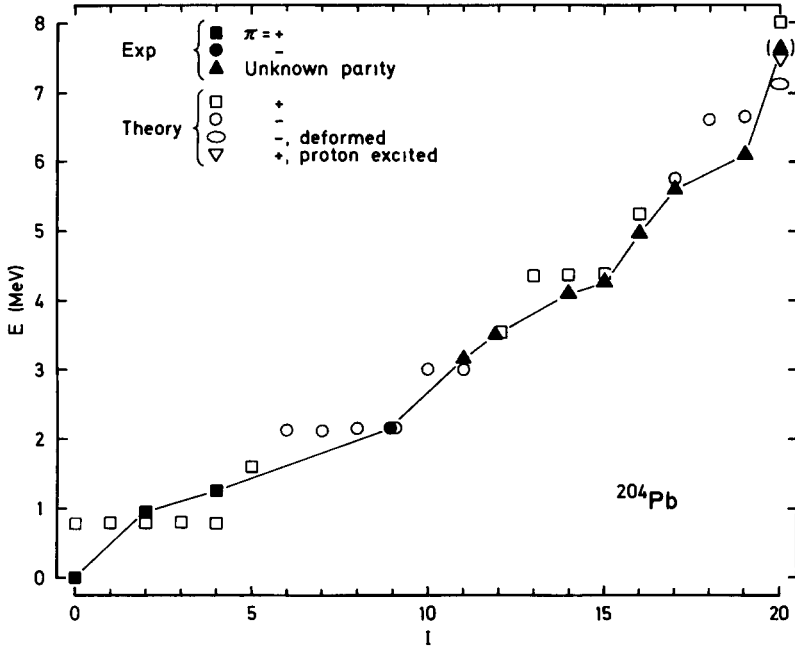
or pure sphere) are then step functions. On the other hand, the plot of energy $E_{s\,p}$ versus I contains only separate points with only the "optimal values" present (marked as open circles in fig. 33). Since the energy jump $E_{s\,p}$ is always positive, the energy $E_{s\,p}$ of the optimal states is an increasing function of I. However, this statement holds only in case of fixed deformation ε as all equations have been derived for the same ε.

Now, let us discuss the states that arise in between the "optimal" values of angular momentum. They cannot be obtained by the procedure described above of summing up the spins and energies for the states below the straight tilted Fermi surface. Still, it is perfectly sensible to search for the lowest energy state for *any* value of angular momentum $I(= I_1)$ In case of a pure independent-particle model the states with angular momenta lying in between the two neighbouring values I' and I'' can be constructed by promoting one or more particles above the tilted Fermi surface and leaving holes below. The "optimal" state plays the role of a vacuum in this formulation If we start for example with the state $I = I''$, we may form the $I = I'' - 1$ state in several ways by creating alternative particle-hole states with
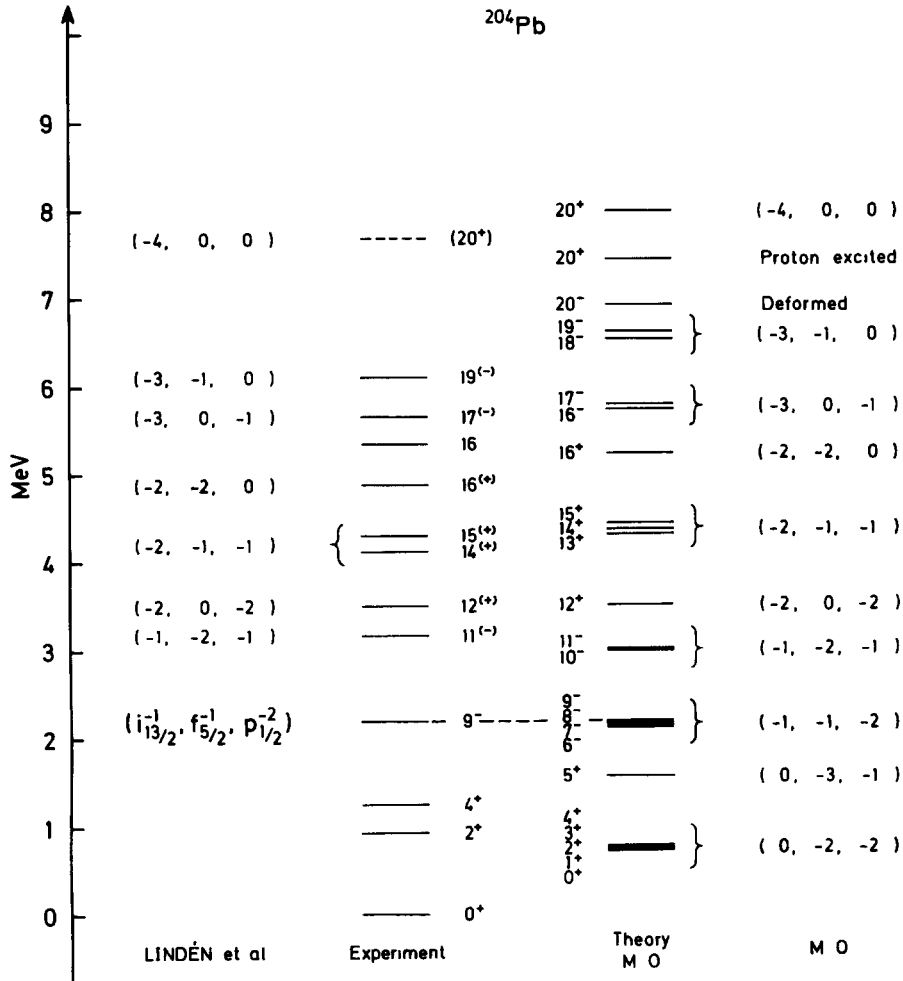
$$m_i^{part} = m_i^{hole} - 1.$$

Fig 36 More detailed comparison of theoretical and experimental spectra of ^{204}Pb An arbitrary fit of the zero-point of the energy scale is made for the 9^- state The fact that the experimental 0^+ state falls lower by a fair amount corresponds to the neglected correlation energy in the 0^+ state The splitting of calculated levels corresponding to identical populations of the spherical *j*-shells is caused by the renormalization of the moment of inertia

One of the states of *n*-particle *n*-hole type corresponds to the lowest energy and can be considered as an yrast state in the pure independent-particle picture (solid circles in fig. 33). In case of the spherical harmonic-oscillator potential the particle-hole states have a very simple structure owing to the high degeneracy in the single-particle levels e_i, as we have seen in fig. 32.

In the case of a more realistic potential such as the modified oscillator, the particle-hole states have been calculated in a detailed way allowing, for the configura-
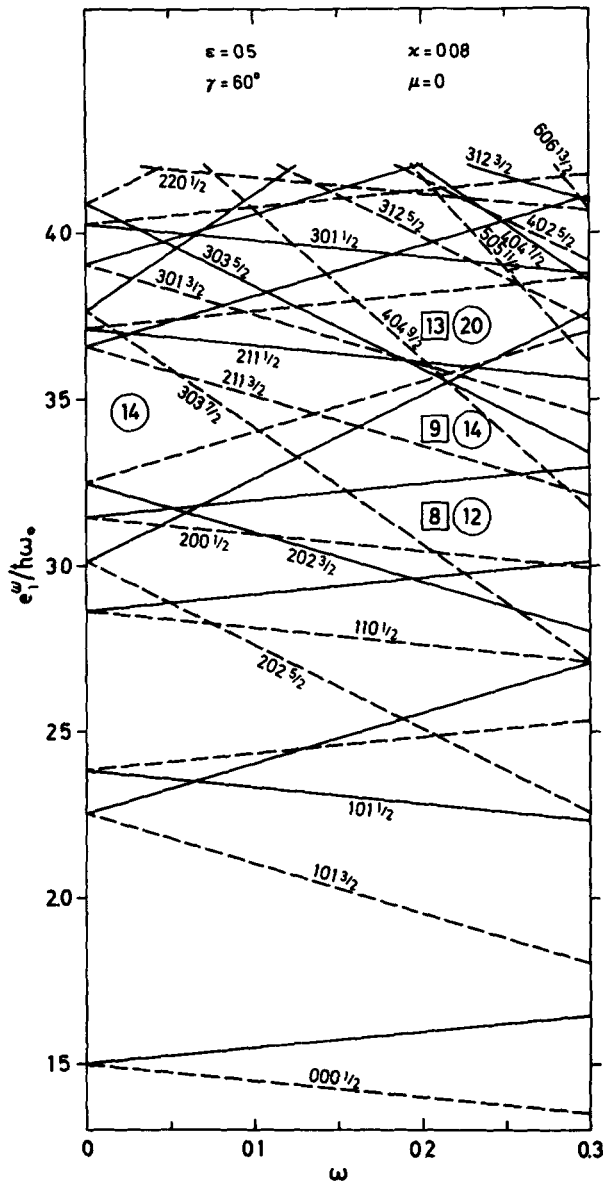
Fig 37 Single-particle diagram of e_i^ω rotational frequency ω, valid in the (s, d) shell for $\varepsilon = 0\,5$, $\gamma = 60°$
According to the rough formula developed in sect 8 a shell structure is expected for $\omega/\omega_0 = 0\,16 \pm 0\,08 = 0\,08$ or $0\,24$ For $\omega/\omega_0 \approx 0\,24$ there are rather distinct shell closures at nucleon numbers 12, 14 and 20 with listed spins For the nuclei ^{24}Mg, ^{28}Si and ^{40}Ca the prediction is thus of particularly stable configurations associated with spin-16 for ^{24}Mg, spin-18 for ^{28}Si and spin-26 for ^{40}Ca

Fig 38 Diagram of the shell energy, E_{shell}, for ^{24}Mg in terms of deformation ε (pure prolate and oblate shapes) and spin-I Note the prolate ground-state minimum being washed out with increasing I and the occurrence of a deep local oblate minimum for $I \approx 16$ and $\varepsilon = -0.5$

tion considered, for the change in deformation along the line of $\gamma = 60°$ The result is shown in fig. 34 for the two nuclei ^{150}Gd and ^{158}Yb. For each spin the yrast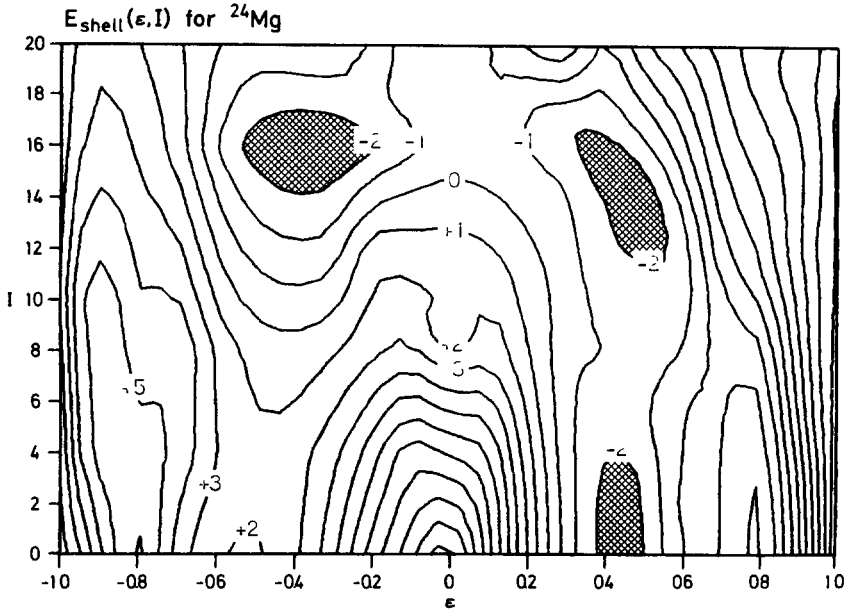 state (and sometimes an additional state) is shown in the figure. Calculations have been performed for all nuclei with part of their trajectory along the oblate axis. The nucleus ^{150}Gd represents the most promising case. As with the MO potential the scale of the rise of energy with I is too small (i e. the inertia value too large), one may also expect that shell fluctuations are underestimated (see the appendix). Larger shell effects would imply more yrast traps.

The "optimal" yrast states are encircled. As stated before, "optimal" refers to the fact that the states are obtained for a given deformation (close to the minimum-energy deformation) when the sloping Fermi surface is a straight line versus ω) One-particle one-hole and two-particle two-hole excitations relative to the "optimal" states are calculated; to denote parity they are marked by $+$ and $-$ All states I that are lower in energy than the generated lowest $I-2$ and $I-1$ states are considered "traps" and marked by dashed vertical lines on their immediate left.

In addition, "traps" can arise for cases when none of the energy-allowed transitions to $I-2$ and $I-1$ states are of 1p1h character, but e.g. of 2p2h type. For each yrast state that is not a trap the arrows mark a possible decay mode of 1p1h character. Such a decay may not always populate states along the yrast line.

Of particular interest are traps at spins 32, 27 and 26 in ^{150}Gd. Predictions of spin

traps of lower I are additionally uncertain because of the neglect of pairing. Also the determination of higher-spin traps is highly delicate. The figures should mainly be taken as *quantitative illustrations* of a more qualitative prediction. We thus consider our results mainly to be relevant as to the question in which regions of mass and spin, traps are most likely to occur.

The fact that traps seem very rare above spin 30–40 is connected with the rapid rise in the average rotational energy with increasing spin. This energy varies with I as I^α, where α is smaller than, but rather near to, two in this region of spin.

Other good oblate spectra are provided by nuclides close to ^{208}Pb. As an illustration we exhibit the spectrum of ^{204}Pb in figs. 35 and 36 We have here adjusted the zero-point of the theoretical and experimental energy scales so as to give a fit of the level of spin-9. The data are taken from a publication by Lindén et al. [20]. In view of the only fair reproduction of the ^{207}Pb spectrum in terms of the MO model the reproduction of the yrast band in ^{204}Pb is highly satisfactory.

The yrast traps may be associated with regions of low or decreasing density in $g_1(e^\omega)$ [in addition they depend on the spin density $g_2(e^\omega)$]. For light nuclei the occurrence of regions of low $g_1(e^\omega)$ densities can be easily understood For A below 40, the l^2 term in the modified-oscillator potential seems to be less important. Then, the analysis of the high angular momentum states may be performed in the framework of the pure HO potential with the addition of the diagonal part of the spin-orbit term. As indicated in ref [17], the points of most pronounced shell structure are characterized by the condition that the derivatives of energy eigenvalues with respect to quantum numbers are proportional to simple integers In case of an axially symmetric harmonic oscillator, rotating around its symmetry axis, it is convenient to introduce three quantum numbers $n_+ = \frac{1}{2}(n_\perp + \Lambda)$, $n_- = \frac{1}{2}(n_\perp - \Lambda)$ and n_3 in the usual notation [23]. Then the condition is

$$\frac{\partial e_i^\omega}{\partial n_+} : \frac{\partial e_i^\omega}{\partial n_-} : \frac{\partial e_i^\omega}{\partial n_3} = a : b : c,$$

where a, b and c are small integers. Since the eigenvalues e_i^ω are linear functions of the quantum numbers·

$$e^\omega/\hbar\omega_0 = (n_\perp + 1)(1 + \tfrac{1}{3}\varepsilon) + (n_3 + \tfrac{1}{2})(1 - \tfrac{2}{3}\varepsilon) - 2\kappa\Lambda\Sigma - \omega\Lambda$$
$$= (n_+ + \tfrac{1}{2})(1 + \tfrac{1}{3}\varepsilon - \omega - 2\kappa\Sigma) + (n_- + \tfrac{1}{2})(1 + \tfrac{1}{3}\varepsilon + \omega + 2\kappa\Sigma) + (n_3 + \tfrac{1}{2})(1 - \tfrac{2}{3}\varepsilon),$$

it is easy to solve the above equations for deformation ε and rotational frequency ω. The result is

$$-\varepsilon = \frac{3}{2}\frac{2c - b - a}{c + b + a},$$

$$\omega = \left[-2\kappa\Sigma + \frac{3}{2}\frac{b - a}{b + a + c} \right]\omega_0.$$

The most relevant deformations in addition to those of trivial type are therefore
$-\varepsilon = 0.30, 0.75, 0\ 187, 0.50$ and 0.136 corresponding to $(abc) = (122), (123), (233),$
(234) and (344), respectively. The corresponding values for ω depend on the strength
of the spin-orbit parameter κ and on the sign of the spin projection $\Sigma = -\frac{1}{2}$ or $+\frac{1}{2}$
The shell structure shows up separately for $\Sigma = -\frac{1}{2}$ and $\Sigma = +\frac{1}{2}$; the final picture
therefore results as the superposition of the two parts of the spectrum.

Fig 37 gives an example of the plot of eigenvalues e_i^ω versus ω. The deformation
parameter $\varepsilon = 0.5$ (with $\gamma = 60°$) is chosen so as to facilitate the analysis of the
structure of the $(abc) = (234)$ configuration. For the pure oscillator case, shell
structure occurs for $\omega = 0\ 167\omega_0$. With a diagonal $l \cdot s$ term this is modified to
$\omega_{\uparrow\downarrow} = (0.167 \pm \kappa)\omega_0$ [in this case $\omega_\downarrow = 0.09\omega_0$ $(\Sigma = -\frac{1}{2},$ solid lines) and
$\omega_\uparrow = 0.25\omega_0$ $(\Sigma = \frac{1}{2},$ dashed lines)]. In the exact calculations the main gaps are
found at $\omega \approx 0.22\omega_0$; the low-frequency shell structure appears to be washed-out
on the other hand The survival of the high-frequency shell structure appears some-
what accidental. In particular, one would *a priori* tend to predict rather well
established states of total angular momentum $I = 26$ in ^{40}Ca, and $I = 16$ in ^{24}Mg,
taking into account equal contributions from neutrons and protons. The resulting
deformation of these states, however, turns out to be somewhat less than $\varepsilon = 0.50$
owing to the influence of the liquid-drop part of the potential energy. The results of
the simplified discussion of the condition of shell structure comes out also in the
exact treatment of the modified oscillator case. Indeed, for ^{24}Mg the shell energy
has a local minimum for $I = 16$ and an oblate deformation $\varepsilon = 0.5$ and $\gamma = 60°$
as seen in fig. 38.

Appendix

THE ROTATIONAL MOMENT OF INERTIA

We define the "dynamical" moment of inertia J_{dyn} as that obtained from the slope
of the line $\tilde{E}$ versus $\tilde{I}^2$ (sect. 4). In the following we will also refer to a "static" moment
of inertia

$$J_{stat} = M \sum_\nu \langle \nu | x^2 + y^2 | \nu \rangle,$$

and furthermore to the "geometrical" or "macroscopic" moment of inertia as that

of a homogeneous mass distribution inside an equipotential surface:

$$J_{\text{geom}} = B_J \frac{4Mr_0^2}{5\hbar^2} A^{5/3},$$

where the shape factor B_J is normalized to unity for a spherical shape. It was first recognized by Bohr and Mottelson [21]) that, for non-interacting fermions in a potential $V(r)$, certain approximations lead to the result

$$J_{\text{dyn}} = J_{\text{stat}}$$

For a more detailed discussion of this theorem see e.g. ref. [14]). In the present calculation it was found instead for the MO potential that

$$J_{\text{dyn}} \approx 1.3 J_{\text{stat}}.$$

Therefore the average spin dependence of the energy has been renormalized to correspond to the macroscopic moment of inertia I_{geom}, in analogy with the renormalization of the deformation dependence to the liquid-drop formula. In the remainder of this appendix we will discuss the cause for the discrepancy between between J_{dyn} and J_{stat} in the MO potential. All numerical results that are presented pertain to medium-heavy nuclei, i.e. with $A \approx 160$

The source of the inertia anomaly in the MO potential is the velocity-dependent l^2 term, as pointed out e.g. in refs [7,14]). This can be seen in the Thomas-Fermi approximation by adding the l^2 term to the kinetic energy in the standard formula [17]) for the moment of inertia. A straightforward integration over the momentum space coordinates then gives

$$J = \int \int \int M_{\text{eff}}(r)(x^2 + y^2)p(r)\mathrm{d}^3 r,$$

which differs from J_{stat} by the appearance of an effective mass

$$M_{\text{eff}}(r) = \frac{M}{1 - 2M\mu'\hbar\mathring{\omega}_0 r^2} \geqq M,$$

where $\mu' = \kappa\mu$. The numerically determined ratio $J_{\text{dyn}}/J_{\text{stat}}$ in an appropriately modified-oscillator potential is accounted for by the formula above in a qualitative way, both as regards the magnitude and the deformation dependence [14]).

In the MO potential, however, there also enters a correction term to l^2. The relevant term is $-\mu'\hbar\mathring{\omega}_0(l^2 - \alpha N(N+3))$, where the strength α is assigned the value $\frac{1}{2}$ in order to fix the centers of gravity of the oscillator N-shells [22]). The l^2 term leads to an increase in J_{dyn}, because it increases both the level density and the average single-particle spin in the vicinity of the Fermi surface, while the renormalization counteracts these effects. As suggested by Mottelson [13]), the latter term can be dealt with in an approximation where sums over quantum numbers are replaced by

integrals. In the limit of small rotational frequencies this gives

$$J_{\text{dyn}} \approx \lim_{\omega \to 0} \frac{1}{\omega} \int_0^\infty dN \int_0^N dl \int_{-l}^{+l} dm \, m \, \theta \, (\lambda_{\text{F}} - N + \mu'(l^2 - \alpha N^2) + m\omega),$$

$$J_{\text{stat}} \approx \frac{2}{3} \int_0^\infty dN N \int_0^N dl \, 2l \, \theta \, (\lambda_{\text{F}} - N + \mu'(l^2 - \alpha N^2)),$$

where λ_{F} is the Fermi energy in units $\hbar\omega_0$. Realistic rotational frequencies affect J_{dyn} and J_{stat} by less than 1 %. After Taylor expansions of the integrands, the integrals can be evaluated as infinite power series in the quantity $\lambda_{\text{F}}\mu'$. For $\alpha = \frac{1}{2}$, the ratio $J_{\text{dyn}}/J_{\text{stat}}$ is about 1.26, in fair agreement with the numerical result. The surprising result is that for $\alpha = 1$ the power series are identical to all orders. In fact, from the integrals above one obtains the closed expression ($\alpha = 1$)

$$J_{\text{dyn}} = J_{\text{stat}} \approx \frac{1}{36\mu'^4} \left[(1 + 4\lambda_{\text{F}}\mu')^{\frac{3}{2}} - 1 - 6\lambda_{\text{F}}\mu' - 6(\lambda_{\text{F}}\mu')^2 + 4(\lambda_{\text{F}}\mu')^3 \right];$$

where λ_{F} is determined from the number of particles $\mathcal{N}$ by

$$\mathcal{N} = \frac{1}{12\mu'^3} \left[1 + 6\lambda_{\text{F}}\mu' + 6(\lambda_{\text{F}}\mu')^2 - (1 + 4\lambda_{\text{F}}\mu')^{\frac{3}{2}} \right].$$

At this point it should be remarked that the power series diverges when $\lambda_{\text{F}}\mu' > \frac{1}{4}$. To employ a modified potential with $\alpha = 1$ the phenomenological $l \cdot s$ and l^2 strengths must of course be redetermined; e.g. a preliminary fit to the experimental single-particle levels in the ^{208}Pb region gave (under the assumption of $\alpha = 1$).

$$\kappa_{\text{p}} = 0.07, \qquad \mu_{\text{p}} = 0.7, \qquad \kappa_{\text{n}} = 0.06, \qquad \mu_{\text{n}} = 0.3,$$

With this potential the single-particle levels are fitted about equally well near ^{208}Pb as in the $\alpha = \frac{1}{2}$ case. In favour of using the renormalization strength $\alpha = 1$ one may remark that this modification also has the appealing property of making the MO potential non-singular (if $\alpha < 1$ the energy of levels with high angular momentum tend to minus infinity). However, this singularity is normally taken care of by a cut-off of the basis, and the reduced renormalization strength $\alpha = \frac{1}{2}$ leads on the whole to a better description of the single-particle levels near the Fermi surface of rare earth and actinide elements.

A few words should be added concerning the prescription used by Neergaard *et al.* [7]), namely to restore J_{dyn} to J_{geom} by the choice of a larger value of the oscillator frequency $\hbar\hat{\omega}_0$. Firstly, this gives an unphysical value for J_{stat}. Secondly, in order to have J_{dyn} equal to J_{geom} not only for the composite nucleus but also for protons and neutrons separately, it would be necessary to apply different renormalizations on $\hbar\omega_{\text{p}}$ and $\hbar\omega_{\text{n}}$ because $\mu_{\text{p}} > \mu_{\text{n}}$. Thirdly, it is clear from the discussion above, and it can been verified numerically by comparison with single-particle levels e.g. in a Woods-Saxon potential, that the effect of the l^2 term on the moment of inertia

is partly due to the fact that the compression of the spectrum is anisotropic with regard to angular momentum. Correcting for this effect will introduce qualitative changes in the behaviour of the shell correction energy at high spins, whereas an isotropic decompression merely changes the energy scale.

Another means of bringing the ratio J_{dyn}/J_{stat} closer to unity is to crank not only the static potential but also the l^2 term. Naively this would seem to be a straight-forward transformation of such a velocity dependent interaction However, the l^2 term is more intended as a simulation of a radial correction term. As such, its transformation is highly unclear Treating the l^2 term straightforwardly, let us examine the rough approximation

$$l^2 \approx r^2 p^2.$$

The cranking Hamiltonian becomes

$$H^\omega = H^0 - \hbar\omega I_x\{1 - 2(1-\alpha)M\mu'\hbar\mathring{\omega}_0 r^2\}.$$

The modification consists in the appearance of the quantity in curly brackets, which multiplied with ω can be thought of as an effective rotational frequency $\omega_{eff} \lessgtr \omega$. The factor $1 - \alpha$ stems from the assumption that the renormalization term transforms in the same way as l^2. It is then trivial that J_{dyn} equals J_{stat} for $\alpha = 1$ On the other hand, for $\alpha = 0$ we get

$$J_{dyn} = \frac{I}{\omega} = \left\langle \frac{I}{\omega_{eff}} \frac{M}{M_{eff}} \right\rangle \approx J_{stat},$$

where the Thomas-Fermi result has been used This latter method does not reproduce numerical results quantitatively, so that except for $\alpha = 1$, J_{dyn} may deviate appreci-ably from J_{stat}. For $\alpha = \frac{1}{2}$ the value of J_{dyn} is 15 % too small Although an "exact" treatment of the l^2 term is quite feasible, we will presently be content to ascertain that the shell correction energy is reasonably insensitive to the choice of cranking Hamiltonian. It emerges that the shell corrections obtained from the employment of the "cranked" l^2 term exhibit a similar dependence on I as before, with oscillations having roughly the same magnitude and a relative displacement $\lesssim 10\hbar$.

The renormalization of J_{dyn} to J_{geom} is prompted by the assumption that both are equal to J_{stat}. The theorem that $J_{stat} = J_{dyn}$ can be questioned on the following grounds. Firstly, its derivation invokes the Fermi approximation within the frame-work of a statistical approach. Using the Kirkwood expansion method, Brack and Jennings [14] find that the lowest-order semi-classical correction contributes < 1 % to J_{dyn} Secondly, there is the effect of non-central forces in the nuclear potential Neergaard et al [7] estimate that spin polarization contributes $2.2A^{-\frac{1}{3}}$ times the moment of inertia J. Thirdly, it is not clear what number of particles is required to justify the statistical approach. For a pure harmonic oscillator the integrals for J_{dyn} and J_{stat} are always equal [see also ref. [21]]. On the other hand, the corresponding expressions for collective rotations of non-interacting fermions in a $1/r$ potential

give a ratio J_{dyn}/J_{stat}, which approaches unity very slowly with A, attaining a value $\approx \frac{3}{4}$ for particle numbers typical of medium heavy nuclei. In the "realistic" Woods-Saxon potential we find numerical deviations from unity of $\pm 3\%$

The moment J_{stat} may differ from J_{geom} as a result of density redistributions caused by shell effects and by the centrifugal force. Shell effects can contribute up to 2% to J_{stat}. In an infinite potential with steep walls the centrifugal effect gives $\lesssim 1\%$, but in a finite potential it is 3–4 times larger. It is known that these density redistributions will also change the Coulomb energy by several MeV [refs. [23,24]]. However, the experimental evidence in ref. [25] indicates that shell effects on the density are exaggerated in most nuclear models. Furthermore, Neergaard et al. [7] find that for a reasonable macroscopic compressibility coefficient, the centrifugal redistribution is negligible. This suggests that the model-independent quantity J_{geom} may be as realistic an approximation as J_{stat}.

References

1) M V Banaschik, R S Simon, P Colombani, D P Soroka, F S Stephens and R M Diamond, Phys Rev Lett **34** (1975) 892
2) B R Mottelson, Proc of the nuclear structure Symp of the Thousand Lakes, Joutsa, 1970, vol 2, p 148
3) A Bohr and B R Mottelson, Phys Scripta **10A** (1974) 13
4) S Cohen, F Plasil and W J Swiatecki, Ann of Phys **82** (1974) 557
5) R Bengtsson, S E Larsson, G Leander, P Moller, S G Nilsson, S Åberg and Z Szymański, Phys Lett **57B** (1975) 301,
   S G Nilsson, invited paper, 3rd IUPAP Conf on energy and physics, Bucarest Sept 9-13, 1975 p 309
6) K Neergaard and V V Pashkevich, Phys Lett **59B** (1975) 218
7) K Neergaard, V V Pashkevich and S Frauendorf, Nucl Phys **A262** (1976) 61
8) S E Larsson and G Leander, Proc Conf on physics and chemistry of fission, Rochester, NY, (IAEA, Vienna, 1974) p 177
9) J Meyer-ter-Vehn, Nucl Chem Div Lawrence Berkeley Laboratory Annual Report LBL-4000 (1974) p 190
10) W J Swiatecki, private communication
11) A Faessler, K R Sandhya Devi, F Grummer, K W Schmid and R R Hilton, Nucl Phys **A256** (1976) 106,
    A Faessler, M Ploszajczak and K R Sandhya Devi, preprint Julich (1976)
12) B K Jennings, private communication (1974)
13) B R Mottelson, private communication
14) M Brack and B K Jennings, Nucl Phys **A258** (1976) 246
15) W D Myers and W J Swiatecki, Ark Fys **36** (1967) 343
16) S E Larsson, I Ragnarsson, S Åberg and R K Sheline, to be published
17) A Bohr and B R Mottelson, Nuclear structure, vols 1 and 2 (Benjamin, New York, 1969, 1975)
18) A Bohr, Proc Solvay Conf 1970
19) F S Stephens and R S Simon, Nucl Phys **A183** (1972) 257
20) C G Lindén, I Bergstrom, J Blomqvist and C Roulet, Research Institute for Physics, Stockholm, Annual Report, 1974, p 117
21) A Bohr and B R Mottelson, Mat Fys Medd Dan Vid Selsk **30** (1955) no 1
22) C Gustafsson, I L Lamm, B Nilsson and S G Nilsson, Ark Fys **36** (1966) 613
23) P Janecek, Nucl Phys **A253** (1975) 448
24) S E Larsson, G Leander, I Ragnarsson and J Randrup, Proc Nobel Symp, Ronneby, 1974, Phys Scripta **10A** (1974) 65
25) I Sick, J B Bellicard, M Bernheim, B Frois, M Huet, Ph Leconte, J Mougey, Phan Xuan Ho, D Royer and S Turck, Phys Rev Lett **35** (1975) 910